Structural Characterization of Isolated Metal Atoms and Subnanometric Metal Clusters in Zeolites

Lichen Liu,[1] Miguel Lopez-Haro,[2] Jose J. Calvino[2] and Avelino Corma[1*]

[1] *Instituto de Tecnología Química, Universitat Politècnica de València-Consejo Superior de Investigaciones Científicas, Av. de los Naranjos s/n, Valencia, Spain*

[2] *Departamento de Ciencia de los Materiales e Ingeniería Metalúrgica y Química Inorgánica, Facultad de Ciencias, Universidad de Cádiz, Cádiz, Spain*

*Corresponding author. Email: acorma@itq.upv.es

Abstract

The encapsulation of subnanometric metal entities (isolated metal atoms and metal clusters with a few atoms) in porous materials such as zeolites can be an effective strategy for the stabilization of those metal species and therefore can be further used for a variety of catalytic reactions. However, due to the complexity of zeolite structures and their low stability under the electron beam, it is challenging to obtain atomic-level structural information of the subnanometric metal species encapsulated in zeolite crystallites. In this protocol, we would like to show the application of a scanning transmission electron microscopy (STEM) technique that records simultaneously the high-angle annular dark-field images (HAADF) and integrated differential phase contrast images (iDPC) for structural characterization of subnanometric Pt and Sn species within MFI zeolite. The approach relies on the use of a computational model to simulate results obtained under different conditions where the metals are present in different positions within the zeolite. This imaging technique allows to obtain simultaneously the spatial information of heavy elements (Pt and Sn in this work) and the zeolite framework structure, enabling us to directly determine the location of the subnanometric metal species. Moreover, we will also present the combination of other spectroscopy techniques as complimentary tools for the STEM-iDPC imaging technique in order to obtain global understanding and insights on the spatial distributions of subnanometric metal species in zeolite structure. These structural insights can provide guidelines for rational design of uniform metal-zeolite materials for catalytic applications.

1. Introduction

The rational design of heterogeneous metal catalysts requires that the detailed structure of the supported metal entities at molecular and atomic level is known. In recent years, the fundamental studies carried out on isolated metal atoms and metal clusters with a few atoms supported on solid carriers have deepened our understanding on the structure-reactivity relationship[1-3]. There is no doubt that one important driving force for the recent progress in this field is the development of advanced characterization techniques that allow direct visualization of the structure of the supported metal catalysts with atomic resolution[4,5]. Another driving force is the development of new methods to prepare metal catalysts with well-defined active sites, serving as model catalysts for fundamental studies[6-8]. These two aspects can work in a synergistic way and contribute to the generation of new knowledge on the nature of the active sites in heterogeneous metal catalysts.

Numerous recent studies have demonstrated that supported subnanometric metal catalysts (including both isolated atoms and clusters) on conventional open-structure carriers may sinter into large nanoparticles under harsh reaction conditions, especially in reductive atmosphere (e.g., CO, H_2, CH_4 etc.)[9-11]. This is unfortunate, because these reagents are the ones that are commonly encountered in reactions that these materials are used as catalysts. Therefore, developing new synthesis methodologies to improve the stability of subnanometric metal catalysts is crucial for pushing them to practical applications. In a recent work, we have developed a new synthetic method to generate singly dispersed metal atoms and subnanometric metal clusters at specific locations inside the zeolite structure. This method allows us to prepare highly uniform metal-zeolite materials, in which those confined subnanometric metal species are highly stable against high temperature sintering (up to 650 ^oC in H_2)[12].

The materials prepared by our method with subnanometric PtSn bimetallic clusters selectively located in the 10MR sinusoidal channels of pure-silica MFI zeolite show high activity and stability for an industrially important reaction, the dehydrogenation of propane to propylene (Box 1). Compared to supported metal catalysts on conventional solid carriers (such as carbon, metal oxides, etc.), metal species confined in zeolites, or generally speaking, in porous materials, are more difficult to characterize, especially when one needs to obtain the structural information at atomic level[13-15]. From a structural point of view, the geometric structure of a subnanometric metal entity (isolated atom or

cluster) is directly related to its surrounding environment. It can be expected that, when a metal atom/cluster is located in different positions within the zeolite structure, the geometric structure of the metal entity will be different, and that this will influence its catalytic behaviour. Taking into account the porous matrix, the accessibility of the metal entity could also be modified, which can be associated to the shape-selective reactivity. Therefore, clarifying the exact location of metal atoms and clusters within the zeolite structure is critical to elaborate a model to describe the coordination environment of the metal entities. With this information in hand, the establishment of structure-reactivity relationship will be possible.

As summarized and compared in **Table 1** and **Table 2**, transmission electron microscopy (TEM) variants are the most frequently used techniques to directly study the morphology, particle size and chemical composition of solid catalysts[16,17]. Compared to other microscopic imaging techniques, TEM/STEM can offer the possibility to study zeolite materials with atomic resolution[18-22]. Regarding metal-zeolite materials, it has been shown in the literature that, it is readily possible to image single atoms (such as Au, Ir, Rh, Pt, etc.) and clusters containing a few metal atoms located inside zeolite crystallites by aberration-corrected scanning transmission electron microscopy (AC-STEM)[23-25]. However, the contrast of the zeolite framework is usually quite low in the high-angle annular dark-field (HAADF) imaging mode of AC-STEM, making it very difficult to identify the exact position of atoms and clusters in the zeolite structure. Using TEM, it is necessary to obtain two images: one optimized for zeolite structure, one optimized for determining the position and shape of the metals or metal clusters.

In fact, direct imaging of zeolite structures with atomic resolution, has been usually carried out in transmission mode (HRTEM), since phase contrast allows visualizing, with adequate signal/noise ratio, all the light elements (Si, Al and O) in the zeolite framework[26-28]. However, zeolites are usually quite sensitive to electron beam and the materials could be partially or completely damaged even after taking one TEM or HAADF-STEM image. Therefore, the consecutive imaging in TEM and STEM mode may not work for metal-zeolite materials, especially in the case of samples containing singly dispersed metal atoms, because of the low stability of the singly dispersed atoms under the electron beam[29,30].

The simultaneous imaging of both the metal component and the zeolite structure, which is required to identify the distribution of the metals within the Si-O or Si-Al-O framework is a challenging task.

It requires a novel methodological approach, which spans over both synthetical and characterization aspects. A metal-zeolite material with uniform distribution of metal species inside the zeolite framework should be prepared as the well-defined model material to test the reliability of the new technique. Otherwise, metal species at different locations will be interfere each other in the 2D projected TEM images. Moreover, image simulation studies are also strongly required in order to interpret the experimental images adequately.

In this protocol, we use the synthesis of pure-siliceous MFI zeolite with PtSn bimetallic clusters confined in the sinusoidal channels as an example, to show the workflow for the synthesis and structural characterization of metal-zeolite composite materials with singly dispersed atoms or subnanometric metal clusters confined inside the zeolite structure. The synthetic method is described in Section 2.

To address the challenge mentioned before on identification of the positions of metal atoms in beam-sensitive zeolites, we have developed a combined imaging technique which allows to record high resolution high-angle annular dark-field image (HAADF) for heavy metals (Pt and Sn in this showcase) and integrated differential phase contrast image (iDPC) for the zeolite framework in the same area, simultaneously[31,32]. With these complementary images and the supporting results from image simulation, it is now possible to directly localize the position of a single Pt atom in the zeolite structure by correlating the paired HAADF and iDPC images. It should be mentioned that, this HAADF-iDPC combined imaging techniques can also be extended to other materials such as metal-organic frameworks (MOFs), mesoporous materials as well as other solid crystalline materials. This is discussed on more detail in Section 6 and 7, where we provide advice on how to adapt our approach to the analysis of other types of material that similarly contain a mixture of components some of which are damaged in the course of a single TEM experiment.

Another approach that is often taken to look at the structure and chemical compositions of solid materials is X-ray energy dispersive spectroscopy (X-EDS) or electron energy loss spectroscopy (EELS)[33]. However, when dealing with the beam-sensitive metal-zeolite materials, the low spatial resolution precludes us to achieve that purpose. HAADF-STEM is promising, and we can address 'this particular issue' by performing K-means clustering on the basis of image simulation results. As shown in our recent work, it is possible to get a rough estimation of the respective positions of subnanometric

Pt and Sn species according to their contrast in the high-resolution HAADF-STEM images[12]. We will discuss this in more detail in Section 4. This image analysis approach can also be applied to other systems, in which conventional X-EDS or electron energy loss spectroscopy (EELS) is not able to provide the information on the material's chemical composition.

The presence of isolated atoms and subnanometric metal clusters in zeolite crystallites has also been confirmed by other techniques, such as in situ X-ray absorption spectroscopy, in situ IR spectroscopy and CO chemisorption. These are discussed in more detail in Section 5. By combining these spectroscopic techniques with the electron microscopy approach described above, one can obtain reliable and complementary information on the electronic and geometric structures of the metal species. With all that information, it is now possible to reach a more detailed and global understanding of the structural features of metal-zeolite materials comprising isolated atoms and nanoclusters.

Box 1. Brief introduction on zeolites and their porous structures.

Zeolites are a family of crystalline porous inorganic materials with ordered pores and cavities below 1 nm. Zeolites are usually made with tetrahedrally coordinated atoms (Si, Al and P as the most common tetrahedron-coordinated atoms) connected with oxygen and can be doped with heteroatoms such as Ti, Sn, V, B etc. According to the Structure Commission of International Zeolite Association (IZA), there are ~250 framework types that showing different topological structures. For each type of topological structure, a framework type code has been assigned (see http://www.iza-structure.org/databases/). For instance, ZSM-5, a widely used shape-selective catalyst in chemical industry is named as MFI. The size of the pore, channel or cavity in zeolite structure can be described by the number of tetrahedron atoms. In the case of MFI zeolite, it contains two types of 10 member-ring (MR) channels, i.e. 10MR straight channel (5.3 Å × 5.6 Å) and the 10MR sinusoidal channel (5.1 Å × 5.5 Å). The crossing of the two types of channels gives to an intersectional void of ~7 Å. Molecules and reactants can diffuse through these channels and the unique porous structure of MFI zeolite makes it as one of the widely used zeolite materials in chemical industry. As shown in the figure below, the three types of microporous channels/pores can be visualized by high-resolution TEM along different crystal orientations.

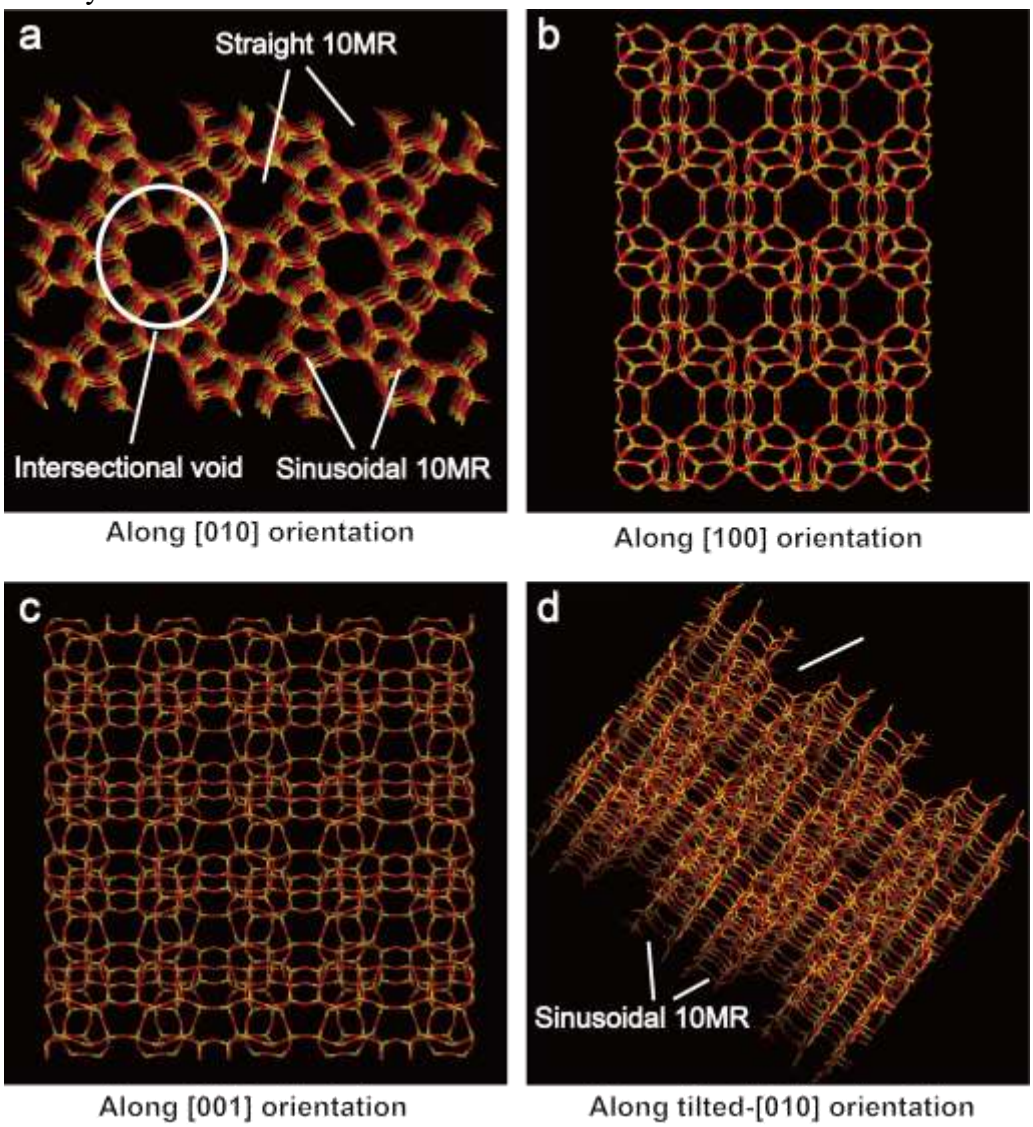

Box 2. Subnanometric metal catalysts supported on solid carriers.

Heterogeneous metal catalysts can be briefly categorized into three types: supported isolated atoms, metal clusters and nanoparticles. By considering the chemical composition, bimetallic and multi-metallic entities are also widely involved in both fundamental studies and industrial applications. In the figure shown in this box, several typical types of metal entities supported on conventional open-structure solid carriers (SiO_2, TiO_2, Al_2O_3, carbon, etc) (see Panel **a**). Those metal entities are located on the external surface of the support.

When the solid carrier is changed to porous materials such as zeolites and MOFs, the metal entities will be stabilized in a confined space where the metal entities are surrounded by the framework. In this scenario, the structures (both electronic and geometric) of the metal entities and their accessibility will be influenced by the location of the metal entities. Taking Pt clusters encapsulated in MFI zeolite structure as an example, Pt cluster can be located in three possible locations: intersectional void, straight channel and the sinusoidal channel, as illustrated in (b). By directly measuring the structure of the Pt-MFI material by high-resolution STEM, it will be possible to determine the exact location of the subnanometric Pt species since the projection image along various crystal orientations will be different, as shown in **Box 1**.

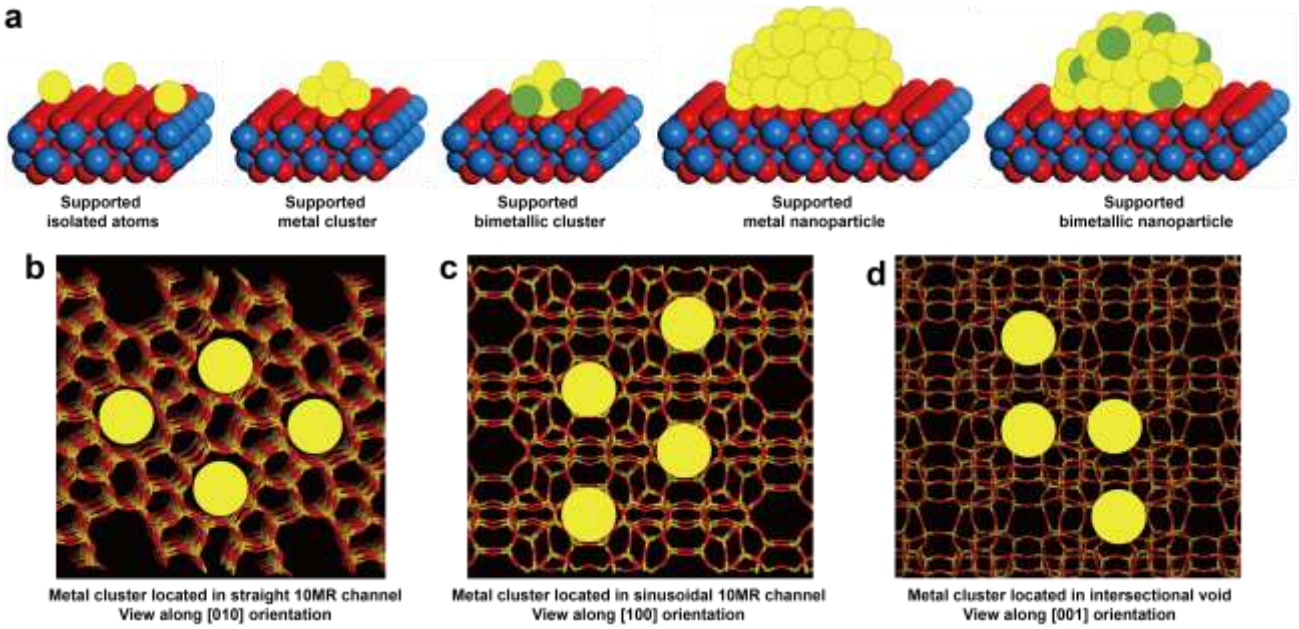

Table 1. Imaging techniques frequently used in the literature for structural and morphological characterization of zeolite materials.

Zeolite Structure (IZA Code)	Imaging technique	Information obtained	Reference
MFI	FESEM	Morphology of the mesoporous zeolite crysallites	16
MFI	AFM	Growth mechanism of Silicalite-1	17
BEA, MFI, MEL	TEM	Zeolite structure	18
Au-FAU Ag-LTA	STEM	Location of metal atoms within the zeolite structure	19, 20
Pt-MFI	STEM-iDPC	Exact location of Pt atoms and clusters within the zeolite structure	This work

Notes: Field-emission scanning electron microscopy (FESEM), Atom-force microscopy (AFM), transmission electron microscopy (TEM), Scanning transmission electron microscopy (STEM) and STEM-iDPC (Scanning transmission electron microscopy and integrated differential phase contrast imaging). In this table, MFI, BEA, MEL, FAU and LTA are structure codes corresponding to different zeolite topological structures, as referred to the Structure Commission of International Zeolite Association (IZA).

Table 2. Comparison of different imaging techniques for the characterization of zeolite materials.

Imaging technique	Advantage	Disadvantage
FESEM	■ Fast image acquisition ■ Allow to obtain general morphological information of the sample ■ Low damage to the sample ■ Easy sample preparation ■ Applicable to a wide range of samples	■ Low spatial resolution ■ Information limited to the external morphology
AFM	■ Allow in situ measurements ■ Low damage to the sample ■ Allow to study electronic properties of flat sample	■ Limited to flat sample ■ Information limited to the external morphology ■ Long image acquisition time
TEM	■ High spatial resolution ■ Short image acquisition time ■ Applicable to a wide range of samples	■ Local structural information ■ Unable to differentiate heavy elements from the zeolite framework ■ Beam damage to the sample
STEM	■ High spatial resolution ■ Allow the differentiate heavy elements from the zeolite framework ■ Applicable to a wide range of samples	■ Local structural information ■ Difficult to work with thick samples ■ Long image acquisition time
STEM-iDPC	■ High spatial resolution ■ Allow the differentiate heavy elements from the zeolite framework ■ Applicable to a wide range of samples ■ Low beam damage to the sample ■ Allow to identify the location of the heavy elements within the zeolite structure	■ Local structural information ■ Difficult to work with thick samples ■ Moderate to long image acquisition time

Notes: Field-emission scanning electron microscopy (FESEM), Atom-force microscopy (AFM), transmission electron microscopy (TEM), Scanning transmission electron microscopy (STEM) and STEM-iDPC (Scanning transmission electron microscopy and integrated differential phase contrast imaging).

2. Generation and stabilization of isolated Pt atoms and subnanometric Pt clusters in MFI zeolite

The encapsulation of Pt atoms and subnanometric clusters in MFI zeolite crystallites can be achieved by one-pot synthesis, as illustrated in **Fig. 1**. The presence of K^+ has a significant impact on the size of the Pt particles in the final Pt-zeolite materials, obtained after calcination in air and subsequent reduction treatment by H_2. In this section, we will describe a detailed procedure for the synthesis of Pt-zeolite materials with different chemical compositions, with emphasis on the generation of isolated Pt atoms and subnanometric Pt clusters in MFI zeolite.

2.1 Materials

2.1.1 Reagents

- Tetrapropylammonium hydroxide solution (TPAOH-Aldrich, 20 wt% in H_2O, containing K^+ in the solution, supplied by Merck, cat. No. 254533-100G)
- Tetrapropylammonium hydroxide solution (TPAOH-Alfa, 40 wt% in H_2O, not containing K^+ in the solution, supplied by Alfa Aesar, cat. No. 17456.22)
- MilliQ water
- $SnCl_4 \cdot 5H_2O$ (supplied by abcr GmbH, cat. No. AB202652-100 g)
- $H_2PtCl_6 \cdot xH_2O$ (supplied by Merck, cat. No. 81080-1G)
- Tetraethyl orthosilicate (TEOS, supplied by Merck, cat. No. 131903-500ML)
- Ethylene diamine (supplied by Sigma-Aldrich, cat. No. E26266-1L)

2.1.2 Equipment

- Plastic vessel (~50 mL volume)
- Stirring bar
- Plastic pipette
- Weighing balance
- Filter paper
- Drying oven

- Mortar
- Calcination oven connected with air
- Reduction oven connected with H_2 (>99.9% purity)

2.2 Procedure for material synthesis

Taking the preparation of K-PtSn@MFI sample (with ~0.4 wt% of Pt, ~0.9 wt% of Sn and 0.6 wt% of K) as an example, a synthesis procedure is explained step-by-step.

1) **Hydrolysis of TEOS in TPAOH solution.** Mix 2.5 g of TPAOH-Alfa solution (supplied by Alfa Aesar), 3.12 g of TPAOH-Aldrich solution (supplied by Merck) and 8.5 g MilliQ water in a plastic vessel that has a lid to form a solution. Then add 4.12 g of TEOS to the solution. Close the vessel, stir the suspension vigorously for ~6 h at room temperature (~20 ^oC), until the TEOS has completely hydrolysed. A colourless solution will be formed after the hydrolysis of TEOS, though a very small amount of precipitate may form. The eventual appearance of a small amount of precipitate doesn't influence the preparation of Pt-zeolite materials.
2) **Addition of Sn precursor.** Add 50 mg of $SnCl_4 \cdot 5H_2O$ to the solution formed in **Step 1** under stirring. After 5-10 min, the $SnCl_4 \cdot 5H_2O$ will be completed dissolved, resulting in the formation of a clear solution. Considering $SnCl_4 \cdot 5H_2O$ can be corrosive to metals, it is recommended to use plastic spoons.
3) **Addition of Pt precursor.** Add 80 μL of H_2PtCl_6 stock solution (the H_2PtCl_6 stock solution was prepared by adding 5.0 g of MilliQ water to 1 g of $H_2PtCl_6 \cdot xH_2O$ supplied by Merck) to the solution formed in **Step 2** under stirring, resulting in a yellow solution.
4) **Addition of ethylene diamine.** After adding the H_2PtCl_6 solution, inject 150 μL of ethylene diamine. Keep the yellow solution under stirring for 3-5 min.
5) **Transfer to electric oven.** Transfer the yellow solution to a Teflon-lined autoclave (total volume 35 mL) and then place in an electric oven at 175 ^oC. The hydrothermal synthesis was carried out under static conditions for 96 h.
6) **Isolation of the solid product from the autoclave.** After the hydrothermal synthesis, recover the solid product by filtration and then wash with water and acetone. After washing with acetone, dry the sample in air at room temperature for 12 h or at 60 ^oC in an oven. Once the hydrothermal

reaction is completed and the autoclave is cooled to room temperature, the separation of the solid product from the autoclave can be carried out within 3 days. The solid product is stable in the autoclave at room temperature for at least 3 days.

7) **Calcination of the solid product in air.** Calcine the as-synthesized K-PtSn@MFI in air (~50 mL/min) at 560 °C for 8 h, with a ramp of 2 °C/min from room temperature to 560 °C. After this calcination program, cool the sample to room temperature naturally in air flow. After the calcination at 560 °C, calcine the sample again in air (~50 mL/min) at 600 °C for 2 h with a ramp of 5 °C/min from room temperature to 600 °C. After the second calcination, cool the sample to room temperature naturally under air flow, giving to the formation of a sample referred as K-PtSn@MFI-Air sample.
8) **Reduction of the calcined solid product by H_2. Reduce** the K-PtSn@MFI-Air sample by H_2 (~50 mL/min) at 600 °C for 1 h with a ramp rate of 5 °C/min from room temperature to 600 °C. After 1 h at 600 °C, cool the sample to room temperature naturally in H_2 flow, giving to the formation of K-PtSn@MFI sample.

Pause point: Solid products obtained in the above Step 7 and 8 will be used further in the following characterization studies and they can be stored in closed glass vials under ambient conditions at room temperature.

9) **Adjusting the amount of K^+ in the final material.** Since the K^+ in the final Pt-zeolite material comes from the K^+ in the TPAOH solution supplied by Merck, the amount of K^+ in the final product can be adjusted by varying the ratio of the two TPAOH solutions while maintaining the same total amount of the organic structure-directing agent in the synthesis mixture. Roughly, the amount of K^+ in the final Pt-zeolite material can be varied from 0 wt% (when only the K-free TPAOH solution is used) to ca. 1.5 wt% (when only the K-containing TPAOH solution supplied by Merck is used). The amount of K^+ can be further increased by adding additional KCl into the synthesis mixture.
10) **Adjusting the amount of Pt in the final material.** The amount of Pt in the final product can be determined by inductively coupled plasma (ICP) analysis and the Pt loading in the final material can be tuned by the volume of H_2PtCl_6 solution that injected into the synthesis mixture in **Step 3**.

11) **Adjusting the amount of Sn in the final material.** The amount of Sn in the final Pt-zeolite material can be tuned by adjusting the amount of $SnCl_4 \cdot 5H_2O$ added in **Step 2**. Notice that if the amount of $SnCl_4 \cdot 5H_2O$ added is too high, the crystallization of the MFI zeolite under the abovementioned conditions (175 °C, 96 h) could be slower, and some amorphous product after the abovementioned hydrothermal treatment may also be formed.

The synthesis of the other Pt-zeolite materials presented here is similar to the above described procedure, with slight modifications in the amounts of organic structure-directing agents and Sn precursor, as listed in **Table 3**. The results of the chemical composition of the final Pt-zeolite material, as measured by ICP, are gathered in **Table 4**. A trouble-shooting summary is also presented in **Table 5**. The amount of K, Pt and Sn can be adjusted as mentioned above if one wants to study the influence of the chemical composition on the catalytic performance. The variation of each element is dependent on the target reaction and should be optimized on the basis of the reactivity output. We suggest to prepare the starting materials by following our procedure and then optimized the synthesis accordingly (e.g. with a 20-50% change regarding to our procedure).

Table 3. Material specification for the preparation of various Pt-zeolite materials.

Sample	TPAOH-Aldrich (with K^+)/g	TPAOH-Alfa (without K^+)/g	H_2PtCl_6 solution/μL	$SnCl_4 \cdot 5H_2O$/mg	Ethylene diamine/μL
Pt@MFI	-	8.12	80	-	150
PtSn@MFI	-	8.12	80	28	150
K-Pt@MFI	6.24	5.0	80	50	150
K-PtSn@MFI	6.24	5.0	80	50	150

Table 4. Chemical compositions of the Pt-zeolite samples prepared by one-pot synthesis.

Sample	Pt (wt.%)	Sn (wt.%)	K (wt.%)
Pt@MFI	0.43	-	-
PtSn@MFI	0.44	1.0	-
K-Pt@MFI	0.42	-	0.6
K-PtSn@MFI	0.42	0.9	0.65

2.3 Timing for material synthesis

Step 1, ~6 h;

Step 2-4, ~1 h;

Step 5, 72 h;

Step 6, 1-2 h;

Step 7, ~15 h + ~6 h for the two calcination procedures

Step 8, ~6 h

Table 5. Troubleshooting for the synthesis of Pt-zeolite materials.

Step	Problem	Possible reason	Solution
1	After 6 h of stirring, the solution is still not clear and homogeneous.	The hydrolysis of TEOS is not completed.	Extend the time of stirring. After over-night stirring, a clear solution should be formed.
2	It is very difficult to weigh the $SnCl_5 \cdot 5H_2O$ due to the presence of some liquid in the container.	Deliquescence may occur with the compound.	Buy a new one from commercial supplier.
5	Check whether the Teflon-lined autoclave is clean.	Some residual solid products from last synthesis may remain in the autoclave. The impurity may influence the crystallization of the Pt-zeolite material.	Clean the autoclave with HF solution. **Be extremely cautious during the use of HF solution and ensure the use of proper personal protection.**
7	Part of the solid product obtained after calcination in air is grey.	The organic structure-directing agent is not completely removed during the calcination in air.	Carry out the calcination process again and use a higher flow of air.
8	Strong re-oxidation of the reduced Pt-zeolite material in air	Some H_2 is adsorbed by the material and when the sample is taken out from the reduction oven, strong oxidation and heat release may occur.	Use inert gas (N_2 or He) to clean the reduction oven in order to remove most of the H_2 adsorbed on the material

3. Preliminary Characterization of the Pt-zeolite materials

Before carrying detailed structure characterizations, it is suggested to perform preliminary characterizations with the Pt-zeolite powder samples obtained from hydrothermal synthesis. To verify the solid product showing the desired crystal structure, measurement of the powder X-ray diffraction pattern is the most convenient way. Following that, the crystallinity can be evaluated by FESEM. If zeolite materials with good crystallinity is obtained, it is recommended to check the sample further by conventional TEM.

3.1 XRD

To confirm the formation of MFI-type zeolites after the hydrothermal synthesis, perform powder X-ray diffraction (XRD) on the solid powders. In our lab we use a HTPhilips X'Pert MPD diffractometer equipped with a PW3050 goniometer using Cu Kα radiation and a multisampling handler. Typical diffraction patterns of the resultant materials obtained from the above one-pot synthesis are shown in **Fig. 2**. Generally, all the samples showed diffraction patterns of MFI-type zeolite, regardless of the chemical compositions. According to those patterns, the crystallinities of the various Pt-zeolite materials were also quite similar.

If the solid product comprises amorphous silica formed from the incomplete hydrothermal crystallization, the peak intensities in the XRD pattern could be low and a broad band may appear at 20-30^{o} (2theta value).

3.2 Field-emission scanning electron microscopy (FESEM)

After confirming the phase structure of Pt-MFI zeolite materials, their morphology can be studied by FESEM. For zeolite materials, crystallites with regular shapes can be observed by FESEM and the amorphous composition in the solid sample can also be identified as small spherical particles (usually <50 nm). In our lab we use ZEISS Ultra55 FESEM to measure the powder sample directly. As shown in **Fig. 3**, all the samples show typical hexagonal prismatic shape with similar crystallite size of 300~400 nm[28]. It should be noted that, according to these FESEM images, the morphology of the Pt-zeolite materials is quite similar to each other, regardless of the chemical composition[29]. With the

results presented in **Fig. 2** and **Fig. 3**, we can conclude that, the growth of MFI zeolite crystallites seems to be barely influenced by varying the chemical composition of the starting synthesis mixture.

3.3 Conventional TEM

In preparing samples for TEM, there are two points that are really important to consider:

1. The choice of solvent for applying the sample.
2. The choice of grid.

In our work, we suspend the solid samples in CH_2Cl_2 and drop the suspensions directly onto holey-carbon coated copper/nickel grids (300 meshes).

Solvent choice: The choice of CH_2Cl_2 as the solvent is related to its high volatility and capability to disperse zeolite powders under ultrasonication. Other solvents such as ethanol, n-hexane or even water may alternatively be used. Since zeolites are porous materials, it may require a long time for the complete evaporation of the solvent. Therefore, we suggest to leave the grids drying under a lamp overnight before the TEM measurements to avoid contamination by organic solvent residues retained within the pores of the zeolite.

TEM grids: The use of proper TEM grids is really important to the success of the experiment. In this work, we chose holey-carbon coated copper/nickel grids (300 meshes), since the MFI zeolite crystallites can be well dispersed on the carbon film with a high possibility to be in the [010] orientation. We have tested other grids such as the holey-carbon coated copper grids (200 meshes) or lacey-carbon coated copper grids, but we encountered problems caused by the charging of the specimen when measuring the samples by high-resolution STEM. Under those circumstances, we observed beam drift during recording the STEM images.

To get a general idea on the dispersion and size of Pt species in the Pt-zeolite materials, we use non-corrected JEOL 2100F microscope operating at 200 kV both in transmission (TEM) and scanning-transmission modes (STEM) was used to record High Angle Annular Dark Field (HAADF), Z-contrast, images at low resolution. Once properly aligned, this microscope allows us to visualize Pt nanoparticles (>1 nm) and subnanometric Pt clusters of ~0.5 nm. Isolated Pt atoms in zeolites will not be directly observed in conventional TEM experiments due to the low contrast between Pt atoms and

the zeolite framework. It is essential to improve the contrast by measuring the sample with AC-STEM, which allows to record images with better spatial resolution at atomic level.

As shown in **Fig. 4**, the K-free Pt@MFI-Air sample obtained after calcination in air at 600 ^{o}C consists of Pt nanoparticles with an average size of ~4 nm, which can be clearly visualized in the low-magnification STEM images. However, if potassium is used in the synthesis of the corresponding Pt-zeolite material, there is much better dispersion of the Pt. As can be seen in **Fig. 5**, no Pt nanoparticles can be seen in the low-magnification STEM images. We know that they are present, because…, so they must be really small and highly dispersed. The critical role of alkaline metals (K in this work) has been discussed in our previous work, where we found that it was associated with neutralization of the silanol groups in MFI zeolite and formation of stabilized -O-Pt species during the calcination in air at 600 ^{o}C[12,36].

As mentioned in the material synthesis section, reduction treatment with H_2 at 600 ^{o}C was carried out with the Pt-zeolite materials to obtain metallic Pt species encapsulated in the zeolite. For the K-free Pt@MFI sample obtained after reduction by H_2 at 600 ^{o}C, representative STEM images obtained with the JEOL-2100F have been gathered in **Fig. 6**. In this case, Pt nanoparticles with a size distribution similar to that of the K-free Pt@MFI-Air sample are observed. Notably, in the case of the K-Pt@MFI-H_2 sample obtained after reducing the K-Pt@MFI-Air sample by H_2 at 600 ^{o}C, subnanometric Pt clusters with uniform distribution in the zeolite crystallites are observed in the STEM images (see **Fig. 7**), this revealing the crucial role of K in the stabilization of tiny Pt clusters. The K-free PtSn@MFI and K-PtSn@MFI samples have also been checked by conventional STEM and the size distributions of Pt particles are similar to that observed with the Sn-free materials (see **Fig. 8**).

However, the position of the subnanometric Pt clusters cannot be determined from the above electron microscopy results due to their limited spatial resolution. Therefore, in order to get a deeper insight into the atomically dispersed Pt species and subnanometric Pt clusters, we have employed aberration-corrected high-resolution STEM (HRSTEM)[37].

Table 6. Summary of the parameters for the optimization of the STEM-iDPC set-up.

Parameters	Optimization range
Beam current	10-30 pA
Convergence angle	18.6 mrad
Camera length	90-115 mm
Dwell time	0.625-2.5 μs
Magnification	1-2 M for imaging of metal clusters and ~2.5 M for imaging of single atoms
Image Size	1024 × 1024 or 2048 × 2048

4. Structural Characterization of the Pt-zeolite materials by HRSTEM

The structural characterization of the Pt-zeolite materials by HRSTEM is carried out by recording HAADF and (integrated differential phase contrast) iDPC images, simultaneously. iDPC-STEM imaging is a recently-developed technique which provides atomically resolved images with the contrast proportional to the atomic number (Z) of the elements, instead of the roughly Z^2-dependent contrasts obtained in HAADF-STEM images.

4.1 Image acquisition by STEM

The iDPC imaging technique is based on the two-dimensional integration on the images obtained with the using a segmented detector with 4 quadrants, which yields a scalar image related to the sample's phase shift and the projected electrostatic potential field within the sample.[31] Notably, the signal-to-noise ratio in iDPC-STEM image is quite high even under very low-dose conditions. Therefore, this technique allows to image light elements, like O, Al or Si, which are used for constructing the framework of some beam-sensitive porous materials such as zeolites. Following the

workflow in **Fig. 9** and referring to the summary of the parameters for the optimization of the STEM-iDPC set-up (**Table 6**), the structural characterization of Pt-zeolite materials prepared by one-pot synthesis by STEM-iDPC technique is shown as an example.

Step 1. Set up the microscope for recording HRSTEM images.

In our lab, HRSTEM images are recorded on a double aberration corrected (AC), monochromated, FEI Titan Themis 60-300 microscope working at 300 kV. This microscope is equipped with a High Angle Annular Dark Field (HAADF) and four-segmented Annular Dark-Field detector (DF4). The DF4 detector is the one used to record the iDPC-STEM images. Using a convergence angle of 18.6 mrad and a camera length of 115 mm, high-resolution HAADF and iDPC images paired images are acquired simultaneously. The resulting range of collection angles for the HAADF detector is 49–200 mrad. An image size of 2048×2048 was chosen to balance the information in a single image and the acquisition time for one scan. An automated fine-tuning alignment of A1 and C1 by the OptiSTEM software was employed to improve the final image quality. The beam current and image acquisition time have been optimized according to the stability of the sample under the beam.

Step 2: Optimize the parameters for acquiring HAADF and iDPC images

To acquire high-quality paired HAADF-iDPC images of subnanometric metal species embedded in zeolite crystallites an adequate electron dose (total number of imaging electrons/unit area) must be fixed which balances the effect of beam damage and the contrast between metal entities and the zeolite framework. Such compromise is particularly important in samples with a large percentage of atomically dispersed metal species, in order to avoid beam-induced sintering.

To obtain the optimal electron dose, several key parameters must be properly tuned, including:

1. beam current
2. dwell time,
3. magnification and image size.

In the practice of optimization of the imaging conditions, the abovementioned Step 1 and 2 should be considered first and can be tested with the zeolite crystallites in different areas on the TEM grid by

fixing the magnification to a medium one (e.g. 1.3 M). Usually, it may take 0.5-1 h to figure out the optimized parameters. Once high-quality images can be recorded with a medium magnification, image recording under different magnifications can be tested and the dwell time can be further optimized accordingly. The procedure is discussed in more detail below.

1. **Beam current** Measure the beam current and decide whether to increase or reduce it. The beam current value can be measured directly from the read-out of the FLUE-CAM of the electron microscope, calibrated by the manufacturer. However, an inaccuracy between 20%-50% has been reported by using this method[38]. Alternatively, the beam current can be also measured by the drift tube of the EELS spectrometer, which is an efficient Faraday cup, giving accuracy in the magnitude of 1 pA or better. In the case of monochromated TEM/STEM microscopes, the beam current can be easily tuned by condensing or decondensing the probe with the focus of the monochromator. In this study on the Pt-MFI materials, a beam current of 10-30 pA was used, depending on the samples. For the materials containing isolated Pt atoms, a lower beam current (~10 pA) is recommended in order to avoid beam-induced sintering of Pt atoms into clusters or nanoparticles during the measurement. Use a larger current (~30 pA) if the zeolite crystallite in the target area is thick since higher beam current can give a higher signal-to-noise ratio and thus improve the contrast of the metal species from the zeolite support. For the Pt-MFI zeolite samples studied in this work, 15-25 pA is the mostly used beam current range. This parameter is optimized in conjunction with optimizing the dwell time. In general, if you use a large dwell time, you would need to use a lower beam current.

2. **Dwell time** The dwell time is the time that the probe stays on each pixel while recording the STEM image in a single scan. Together with the beam current, it is the second parameter which determines the number of electrons crossing the sample per pixel in a scan. Hence, it is also a key factor that needs to be optimized. Determine the total exposure time for each pixel by multiplying the dwell time by the number of vertical scans. The total number of electrons crossing each pixel per image results from the product of beam current, dwell time and number of scans. A short dwell time, for a single scan STEM image, may result in a poor signal/noise ratio in the HAADF-STEM images, which may preclude in some cases the detection of the highly dispersed metal phase. However, a long dwell

time may cause irreversible beam damage to the zeolite material. In the case of Pt-MFI materials, we used dwell times in the 0.625-2.5 μs range depending on the beam current values.

3. Magnification and image size The areal dependence of the electron dose is related to two experimental variables: magnification and image size (total number of pixels in the image, e.g., 1024 × 1024 or 2048 × 2048). Magnification determines the size (e.g., in Å) of the imaged area. Then, division of this quantity by image size will give the pixel size (i.e., Å/pixel), which further determines the pixel area (i.e., $Å^2$/pixel). Since the size of metal atoms and clusters embedded in the zeolite framework are below 1 nm, high magnifications must be used, usually in the 1-2 M range, to clearly discriminate them from the background. Magnifications above this range will bring more damage to the zeolite structure due to high electron dose.

In the case of Pt-MFI materials containing Pt nanoclusters, magnifications of 1.3-1.8 M have been used for the acquisition of HRSTEM-iDPC images with an image resolution of 2048×2048 in pixel. To visualize isolated Pt atoms in the sample, slightly higher magnifications are required, e.g. 2.5 M. When the image is recorded at high magnification like 2.5 M, beam current, dwell time or both, must be lowered in order to keep total electron dose low enough to avoid severe beam damage to the zeolite structure, which is the most sensitive component of the system. Dwell time in the 0.625-1.25 μs range are the most frequently used option in our study.

4. Depth of focus or Depth of field Another parameter that needs to optimized is the depth of focus or field. In STEM microscopy, the depth of field (DOF) depends inversely on the probe convergence angle (α), apart from other parameters like geometrical aberrations, chromatic aberration, etc. The particularity of AC-STEM results in the fact that images can be obtained using very large convergence angles, leading to rather small DOF values. In particular, it has been reported that, the depth of field is 8.5 nm when working at our typical conditions (300 kV and α=18 mrad), a value which is much smaller than the thickness of MFI crystallites[39]. This means that only the subnanometric metal clusters or atoms located near to the surface are imaged at a specific defocus setting. In some cases, it is recommended to decrease the convergence angle towards a more parallel electron beam to improve the visualization of metal species concentrated in the internal space of the zeolite crystallites

at the expense of resolution. In any case, this is an important factor that should be considered during recording the STEM images and also in the analysis of the experimental images.

From the experimental point of view, the convergence angle can also be modified by using a smaller C2 aperture (e.g. C2 aperture = 30 μm) or changing the optic setting of the TEM system. In particular, on the Titan Themis STEM, the probe convergence angle in STEM mode is controlled by C2 and C3 condenser system. It is important to mention that this modification could alter the spherical aberration and the probe corrector should be tuned accordingly.

Step 3. Acquire the images. In order to determine the location of isolated metal atoms or clusters in zeolites, HRSTEM images should be taken along different crystallographic orientations of the zeolite structure. The morphology of the zeolite crystallite is related to its crystalline structure. Therefore, a screening at very low-magnification is recommended to select the potential crystallites with desired orientation for high-resolution STEM imaging[40]. Since beam damage effects limit the total exposure time of a crystallite to the electron beam, only fast adjustments on the crystalline orientation by tilting the microscope stage are allowed. In order to acquire a full understanding on the spatial distribution of subnanometric metal species, it is necessary to record images along different crystalline zone axis. We also recommend to check the crystalline structure of the targeted zeolite and compare their three-dimensional models (referring to the IZA website, https://asia.iza-structure.org/IZA-SC/ftc_table.php) with the experimental images during the acquisition of STEM images.

Example Results

We checked beam damage effects on the MFI zeolite structure and the subnanometric Pt clusters by acquiring a series of successive HAADF-iDPC pairs at increasing exposure times on the same areas of a K-PtSn@MFI sample, **Fig. 10**. The total acquisition time of each image was ~6 s. As can be observed from the comparison of the different images, the size of the subnanometric Pt species remain almost unchanged during the four consecutive scans. However, in terms of the zeolite structure, beam damage starts to be observed already in the third scan (see iDPC image in **Fig. 10f**). The MFI zeolite structure was damaged by the electron beam at different spots where amorphous areas can be clearly

seen in the fourth scan (see **Fig. 10h**). Therefore, we can be confident that, under the conditions selected in our studies, damage to the zeolite structure by the electron beam is not significant for at least two successive scans of ca. 6 s, which already allows us to obtain high-quality STEM-iDPC image pairs to simultaneously determine the size and location of subnanometric Pt species.

Of course, to achieve that, we optimized the beam current, dwell time, magnification, image size and orientation of the zeolite crystallites as well as the preparation of the grid for the STEM-iDPC measurement.

All these parameters should be readjusted when measuring other zeolite materials with the STEM-iDPC technique. Thus, although the set of values reported above for these parameters provides a good starting point, some trial and error work will be unavoidable for each specific material. In most of the cases, the experimental conditions are also dependent on the purpose of the measurement and the desired spatial resolution. Nevertheless, the above-mentioned factors in Step 1 and Step 2 (basic set-up, beam current, dwell time and magnification) are the most important parameters to be taken into account during the optimization process. It should be noted that, since different AC-STEM may have different beam system, the optimization of imaging conditions may also depend on the equipment.

4.2 Image Processing – Denoising

To determine the spatial distribution of the metallic species within the zeolite framework, a specific methodology for the digital analysis of the experimental images has been developed and coded in a home-made MATLAB script, which is explained below.

Firstly, to improve the signal-to-noise ratio, the HR HAADF-STEM images were denoised by combining the Anscomb Variance Stabilization Transform (VST) and Undecimated Wavelet Transform (UWT). It is well known that noise in STEM images contain Poisson (shot) type contributions. Therefore, common denoising techniques, which only considers signal-independent Gaussian noise, cannot be used directly. In this regard, the Anscombe Variance Stabilization Transform (VST) is used to transform a Poisson distribution to a Gaussian distribution with variance equal to 1. Then, the UWT can be used to remove the Gaussian noise by performing a two-dimensional decomposition of the image in different scales or coefficients (from the finest to the coarsest one). Such coefficients are named subbands, corresponding to horizontal, vertical and diagonal orientation

of each detail together with a final subband corresponding to the completely smoothed image. It is important to mention that all these subbands are undecimated and have the same size of the original image, providing a redundancy factor of 3J+1, where J is the number of scales used. In this work, the UWT treatment has been applied with B3 splines and J=2 scale, *i.e.* the two first scales are removed. Note that, for a 2048×2048 image size, J=11 scales or coefficients are found. On the other hand, it should be also mentioned that J values smaller than 9 provide blurred images where the fine structural features at atomic resolution are lost.

Box. 3 Workflow for image simulation of supported metal catalyst

Image simulation is a necessary tool for the correct interpretation of experimental STEM images. It can be used to obtain a-priori information about the potential contrasts expected for the objective species on the support under specific measurement conditions[41,42]. Considering the intrinsic low contrast of isolated metal atoms or small clusters consisting of just a few atoms, it is highly recommended to carry out image simulation studies[43].

A typical workflow for STEM image simulation of a supported metal catalyst is shown below. Initially, a model of the support is built starting from its crystallographic information (e.g. the CIF file). The models employed in this work were built using the Rhodius program[44].

Since the STEM images are 2D projections of an actual 3D object, the thickness of the model can be estimated from the lateral particle size observed in the real sample (e.g. from previous conventional TEM, low mag STEM or even SEM studies). Considering that STEM-HAADF image simulation is computationally intensive, the thickness of the model can be sometimes lower than that of the real sample. In spite of that, small models can provide a fast feedback, to check the potential of the selected image recording conditions to reveal the structure of the support. It is recommended to simulate models along different crystallographic orientations in order to correlate with the experimental STEM images on various crystallites.

Once the model of the support is constructed, isolated metal atoms and clusters can be added at the desired locations. The metal/support model, together with the experimental electron-optical parameters characteristic of the microscope and specific imaging conditions used are employed as input to the simulation software. The time required for each simulation depends on the size of the model and the power of the available computation facilities, but it may range from tens of minutes to days.

Once the simulation is completed, the results can be checked and analysed. Random) noise, in particular a mix of Poisson and White Gaussian noise, can also be applied to the simulated image to make them closer to the experimental recordings. Finally, the simulated images can be exported and compared with the experimental ones.

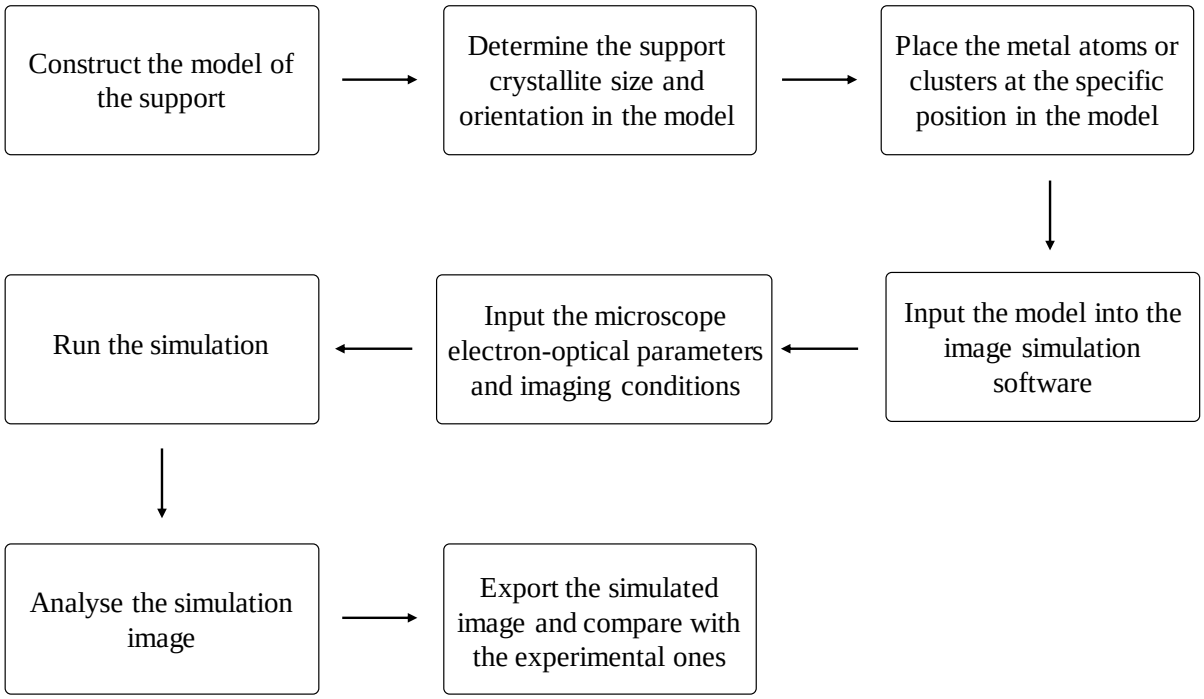

4.3 Image simulation

In HR HAADF STEM images, the image contrast is proportional to roughly the square atomic number (Z^2). Thus, in zeolites consisting of Si and O (Z_{Si}=14 and Z_O=8), it is expected to detect clusters made of heavy atoms like Pt (Z_{Pt}=79) or Sn (Z_{Sn}=50). However, it should be noticed that the contrast of the image changes also linearly with the mass and thickness of the analysed area. Therefore, in systems like MFI zeolites where the thickness is higher than 500 nm, the intensity in the image of Si columns could be even higher than that of both Sn and Pt clusters or single atoms. Likewise, it is well known that the formation of these images can suffer from artifacts, specially electron channelling effects. In this case, some atomic columns can push closer (channel) the electrons in the probe, therefore increasing the fraction of electrons scattered at high angles, i.e., increasing the intensity. Slight deviations from the exact zone axis alignment attenuates channelling.

Hence, to take into account all these factors, HR HAADF-STEM image simulations are essential to correctly interpret the contrasts observed in the experimental images, and also, to provide a priori information to optimize the experimental studies. In this regard, HR HAADF-STEM image simulations have been carried out to provide information about the actual potentials and limits in the following tasks:

1) detection of atomically dispersed metal species;
2) detection of the interaction between subnanometric Pt and Sn cluster and
3) evaluation of the effect of electron channelling in both zone-axis and tilted-zone axis conditions.

Step 1: Create the models. The complex structural models used as input in these simulations were built using the Rhodius software developed at Cadiz University[44]. In particular, supercells in [010] zone axis and [010] off-zone axis have been constructed to evaluate the influence of channelling effects.

Step 2: Set up the software: For our work, all the HR HAADF-STEM image simulations were carried out using TEMSIM software[45]. The optoelectronic parameters used to for the simulations are based on the electron microscope (FEI TITAN^3 Themis 60-300). In particular, HT=300 kV, Cs3=-0.001 mm Cs5=5 mm, convergence angle (α) =18 mrad and detector size = 68-200 and 49-200 mrad where considered respectively. Likewise, in order to take into account the practical working conditions, the

final image simulations have been convolved with a Gauss blur filter implemented in MATLAB.

Use the simulation software to determine detectability of isolated metal atoms in zeolites

Step 1. Create the model. To evaluate the possibility of detecting isolated metal atoms at several possible sites within the MFI zeolite structure in [010] zone axis images, a 50 Å × 50 Å × 50 Å supercell model consisting of Pt or Sn atoms in several plausible positions was constructed. In particular, the straight 10MR channel, sinusoidal 10MR channel as well as the intersectional void were considered.
Step 2. Perform a series of HR-HAADF defocus simulations to study the effect of depth of field on the intensity of metallic atoms at different positions. By changing the parameters in the simulation software, images obtained under different defocus conditions can be obtained.

Example Results

The image simulation results are shown and compared in **Fig. 11 to Fig. 13**. At the straight pore channels or the intersectional crossings, no overlap between the metallic atoms and the zeolite framework takes places, which guarantees, with independence of the image contrast intensity, the detection of individual metal atoms located at these positions. Moreover, the intensities expected for isolated Pt atoms, independently from defocus, are higher than those of Sn, so they could be distinguished from each other. It is also clearly shown that the Pt and Sn atoms at the sinusoidal channels can also be detected and discriminated from the surrounding zeolite framework, at any defocus. Also, in this case, the intensities of Sn atoms are lower than those corresponding to Pt. Therefore, they could also be distinguished from each other in this particular location according to the contrast difference in HAADF-STEM images.

Simulation to evaluate of the effect of incident beam orientation

Step 1: Create the model. To evaluate the effect of electron channelling, a 200Å × 200Å × 50Å supercells in [010] zone and [010] off-zone axis were built, including Pt and Sn in subnanometric clusters as well as single Pt and Sn atoms. By adjusting the orientation of the model, we will be able

to simulated the images obtained with zeolite crystallites in different orientations.

Step 2: Add noise. To approach as close as possible to the experimental imaging conditions, a mixture of Poisson and white Gaussian noise was added to the simulated images.

Step 3: Use the same image processing method that was used to analyse the experimental images to analyse the, on-purpose, noise-corrupted simulated images.

Example Results:

In the case of the simulated HR HAADF-STEM image along the [010] axis, the contrasts corresponding to the Pt clusters are clearly observed (see **Fig. 14**). For the Sn cluster, the intensity is lower, in some case, even down to the contrast level of the zeolite framework. In the case of Pt single atoms, the contrast provided is slightly higher than the zeolite framework while the Sn atom is barely distinguished from the zeolite structure, since the contrast of a single Sn atom at this location should be at the same level as the zeolite framework.

Looking at the simulation for the off-axis model it is clear that it is easier to visualize all the highly dispersed metal species, especially Pt clusters, Sn clusters and Pt single atoms (see **Fig. 15**). This improvement is related to the reduction of electron channelling effects, which are well known to get reduced when the crystals are slightly off-axis. However, in the case of isolated Pt atoms, the signal displayed is close to that of Sn subnanometric clusters, which can induce challenges on the image analysis and will be discussed later in this paper. Finally, it should be noticed how Sn single atoms remain undetectable.

Since the contrast in HAADF-STEM images is proportional to Z^2 (Z corresponds to the atomic number of the element), the low contrast of isolated Sn atoms in the simulated images indicate that isolated metal atoms neither from the first-row elements (e.g., Fe, Cu or Ni) nor second-row elements (e.g. Pd, Rh or Ru), will be very difficult to be distinguished in MFI zeolites in both [010] or tilted [010] orientations due to their weak contrast from the zeolite framework. The identification of isolated metal atoms in zeolite structure can be achievable with heavy elements (e.g. Pt, Au or Ir), whose detectability is improved in tilted orientation conditions. On the other hand, if the zeolite support is switched to ultra-thin materials with a thickness below 3 nm, for instance, single layer of MWW-type zeolite[46], imaging of the isolated atoms of second-row transition metals by HAADF-STEM should be

possible.

Study on the interaction between subnanometric Pt and Sn clusters

To evaluate a possible interaction between subnanometric Pt and Sn species confined in MFI zeolite, structural models comprising subnanometric isolated Pt clusters and Pt clusters having interaction with Sn clusters embedded in the framework of MFI zeolite have been built. Moreover, HR HAADF-STEM images along the directions slightly tilted off the [010] zone axis were also simulated (see **Fig. 16**). The results obtained in these simulations show the presence of asymmetry contrast in the HAADF-STEM images in the case of Pt clusters interacting with Sn.

Although simulations suggest that this asymmetry can appear for Pt clusters in contact with even a single Sn atom, its detection may be rather complicated and at the limits of the analysis of the contrasts in experimental images. However, the situation is much clearer in the case of contacted Pt and Sn clusters. In this case, the asymmetry feature in the contrast of HAADF-STEM image can be clearly detected in the intensity profiles of the images. Indeed, a shoulder appears in the intensity profile for both Pt_6-Sn_6 and Pt_8-Sn_6 clusters.

4.4 Interpretation of paired STEM-iDPC images

On the basis of the image simulation, we have attempted to identify the location of isolated Pt atoms in the K-Pt@MFI-Air sample, which cannot be achieved by conventional TEM. As shown in **Fig. 17a-b**, some bright dots can be clearly identified in the HR HAADF-STEM images recorded along the [010] orientation, which can be ascribed to isolated Pt atoms. By correlating these bright dots in the corresponding iDPC image, the position of the isolated Pt atoms can be determined to be in the sinusoidal channels. The position of Pt atoms can be further confirmed with the images recorded along the tilted-[010] orientation. As can be seen in **Fig. 17c-d**, Pt atoms overlap with the sinusoidal channels in the iDPC image.

The use of paired STEM-iDPC images for the determination of subnanometric metal species in zeolites can be extended to the samples comprising Pt clusters. In the case of K-Pt@MFI sample, as displayed in **Fig. 18a** and **18c**, 0.4-0.6 nm Pt clusters can be clearly observed as high-intensity areas along the [010] direction, while the 10MR straight channels appear as low-intensity pores. However,

due to the weak contrast of the zeolite framework and its sensitivity to electron beam, the detailed structure of MFI zeolite is not well revealed in the HR HAADF-STEM image. Then, by using the newly developed iDPC technique, the atomic structure of MFI zeolite can be recorded simultaneously with the HR HAADF-STEM image under low-dose conditions (see **Fig. 18b**). As presented in **Fig. 18d**, the detailed structure of MFI zeolite can be clearly identified in the iDPC image, even the 5R units in the framework. Since HR HAADF-STEM imaging is more sensitive to heavy elements (Pt in this work), and the structural information of the zeolite framework is finely captured by iDPC imaging, the precise location of subnanometric Pt clusters can be reliably identified by correlating the paired images. The results demonstrate that Pt clusters of 0.4-0.6 nm are preferentially located in the sinusoidal channels. The location of Pt clusters has also been confirmed by STEM-iDPC imaging on a zeolite crystallite with the tilted [010] orientation, showing that the subnanometric Pt clusters overlap with the sinusoidal channels.

Following the same approach, we have studied the location of subnanometric Pt and Sn species in the K-PtSn@MFI sample by paired HR HAADF-STEM and iDPC imaging. As it can be seen in **Fig. 18i-p**, subnanometric Pt and Sn species are also located in the 10MR sinusoidal channels of MFI zeolite, indicating the presence Sn does not influence the preferential location of Pt.

We have also attempted to correlate the simulated images with experimental HAADF-STEM images. As displayed in **Fig. 19**, the particles with high contrast can be ascribed to Pt clusters while the particles with lower contrast are ascribed to Sn clusters. It should be noted that, due to the very low contras of Pt atom and Sn atom, those isolated atoms are not identified. We have to emphasize that, the assignation of isolated Pt atoms and small Sn clusters is a challenging task because of the background signal from the large size of the MFI zeolite crystallites. We expect that, the identification of the subnanometric metal species will be easier with a thinner zeolite support.

4.5 K-means clustering analysis

For nanomaterials containing multiple elements, such as bimetallic nanoparticles, the distribution of the two elements can be clarified by elemental mapping based on X-ray energy dispersive spectroscopy (X-EDS) or electron energy loss spectroscopy (EELS)[47]. **Fig. 20** shows that, according to X-EDS mapping, K, Sn and Pt are distributed in the whole MFI zeolite crystallite. However, due to

the resolution limitation and the very low stability of the Pt and Sn species embedded in MFI zeolite under the beam, it is not possible to determine the relative spatial relationship between subnanometric Sn and Pt. We found it interesting that there was a measurable difference in the contrast for Pt atoms, Pt clusters, Sn atoms and Sn clusters, and have attempted, to use this parameter to discriminate Pt and Sn distributions by a K-means clustering analysis of the high-resolution HAADF-STEM images.

Since Pt atoms and clusters show higher contrast than the Sn atoms and clusters and their difference can be qualitatively estimated according to the image simulation results, a user-independent, fully automated, segmentation of image contrasts by clustering techniques (K-means method) was applied to recognize and classify the metallic entities, which is a requirement to guarantee statistically meaningful and unbiased results.

To test the K-means clustering analysis methodology, we have carried out the analysis with the simulated images. As shown in **Fig. 21**, Sn clusters and Pt clusters can be clearly identified in all cases, regardless of the distribution of noise. However, the identification of single Pt and Sn atoms is more difficult. The Pt single atoms may be identified as Sn clusters due to their similar contrast and Sn single atoms may not be able to be identified from the zeolite framework.

We also tried to correlated the HR-STEM images with the Pt and Sn amount from X-EDS analysis, but it turned out that it is possible to make such correlation directly under our working conditions with our Pt-zeolite materials. As we discussed before, we may only image part of the Pt clusters and Sn species in the selected area due to the limited depth of focus. This strategy could work for thin samples or metal species on the support's surface, in where the chemical composition could be determined by X-EDS and then be used to facilitate the identification of metal species in HR-STEM images.

As shown in **Fig. 22**, subnanometric Pt and Sn species can be identified according to their different contrast in the HR HAADF-STEM images. Then, in the image depicting the distribution of the Pt and Sn species (**Fig. 22b**) after K-means clustering, it is possible to pick out the Pt and Sn species which are in contact, simply by selecting those which fall at a distance shorter than 0.1 nm in **Fig. 22b**. This distance threshold was selected on the basis of the first-shell Sn-O distance found in the EXAFS analysis. As a result, it is possible to estimate the presence of bimetallic PtSn clusters in the K-PtSn@MFI sample made up of two neighboring Pt and Sn units rather than alloyed clusters, as shown in **Fig. 22c**. The statistical analysis shows that, ~40% of the subnanometric metal clusters automatically

detected in the experimental image of **Fig. 22b** fall at a distance below 0.1 nm.

Additionally, in the experimental HR HAADF-STEM images of the K-PtSn@MFI sample, we have found areas showing intensity profiles similar to those observed in simulation results (see **Fig. 16** and **Fig. 23**). The formation of such subnanometric Pt-SnOx interfacial structure indicate that Pt and Sn species in the K-PtSn@MFI sample are not in the form of conventional PtSn alloy nanoparticles.

It should be noted that, the above K-means clustering analysis is a rough estimation on the distribution of Pt and Sn species in the zeolite structure, due to the following reasons. Firstly, the image analysis is based on two-dimensional projection images. This may result in an overestimation of the fraction of bimetallic clusters, since Pt and Sn at different depths may overlap in the STEM image. Secondly, due to the low contrast between isolated Sn atoms and the zeolite framework, the contact between Pt and Sn may not be able to be recognized by the K-means clustering analysis when a single Sn atom interact with a Pt cluster. Thirdly, though the contrast in the HR HAADF-STEM image is also related to the geometric conformation of a subnanometric cluster, it is possible that a Sn cluster with higher atomicity may show similar contrast to a Pt cluster with lower atomicity. Under this circumstance, the chemical composition of the cluster may not be correctly identified by the K-means clustering analysis. Though there are some limitations for this K-means clustering analysis, we think this is an effective way to study the chemical compositions of bimetallic subnanometric metal clusters encapsulated in beam-sensitive materials.

5. Complementary characterization with other techniques

TEM can provide structural information of the metal-zeolite materials with atomic resolution. However, such detailed information may not be able to reflect global information about the sample as a whole. As complementary tools to TEM, spectroscopic techniques can provide average information on the particle size, electronic structure and coordination environment of the metal species encapsulated in the zeolite crystallites. In this section, we are going to show that by combining the information from both electron microscopy and spectroscopic techniques, one can gain deeper understanding on the structure of Pt-zeolite materials. The specific techniques we will cover are:

1. X-ray absorption spectroscopy (XAS)
2. CO-IR

3. Chemisorption with CO or H_2

X-ray absorption spectroscopy (XAS)

Since the subnanometric Pt and Sn species are embedded in the MFI zeolite crystallites, X-ray photoelectron spectroscopy (XPS) cannot be used to measure the chemical states of Pt and Sn due to the very limited penetration of X-rays. Such information can, however, be obtained by X-ray absorption spectroscopy (XAS), and moreover, the coordination environment of Pt and Sn can also be studied by XAS[48].

Results for Platinum: Taking the K-Pt@MFI-Air as an example, the Pt species in this sample are positively charged, as indicated by the X-ray absorption near edge structure (XANES) spectra shown in **Fig. 24a**. In contrast, the K-free Pt@MFI-Air sample presents a XANES spectrum close to metallic Pt foil. Furthermore, the coordination environment of Pt species can be clarified by the extended X-ray absorption fine structure (EXAFS) spectra and the corresponding fit results (see **Table 7**). As shown in **Fig. 24b**, a short-distance contribution (Pt-O) at ~2.0 Å is the predominant feature in the K-Pt@MFI-Air sample. In the case of Pt@MFI-Air, a significant contribution of Pt-Pt bonding at ~2.7 Å can be observed, indicating the formation of Pt nanoparticles. These results are consistent with the TEM characterization results shown before, which indicate the presence of atomically-dispersed Pt species in K-Pt@MFI-Air and Pt nanoparticles in K-free Pt@MFI-Air.

When the Pt-zeolite samples are reduced by H_2, the size and coordination environment of Pt species in the K-Pt@MFI-Air sample change substantially. The low white line intensity in Pt L_3-edge XANES spectrum of the reduced K-Pt@MFI sample (**Fig. 25a**) indicates the presence of metallic Pt after the H_2 reduction treatment. The coordination number of the first-shell Pt-Pt (N_{Pt-Pt}) bonding for K-Pt@MFI sample is ~6.6 (see **Table 8**), corresponding to an average size of ~0.9 nm[49]. Taking into account that the average size of Pt nanoparticles on the external surface and Pt clusters within the zeolite structure is ~2 nm and ~0.55 nm respectively, then ~80% of Pt atoms should be located inside the MFI crystallites as subnanometric clusters (according to the following simple estimation: 80%×0.55+20%×2 ≈0.85 nm). In contrast, the chemical states of Pt species in the K-free Pt@MFI sample remain almost unchanged after the H_2 reduction treatment and the first-shell N_{Pt-Pt} of the reduced Pt@MFI sample is ~10.6. These results are consistent with the STEM images shown in **Fig.**

4 and **Fig. 8g**, where Pt are already in the form of nanoparticles of 4-5 nm and those particles remain stable during the H_2 reduction treatment.

In the cases of PtSn@MFI and K-PtSn@MFI sample, Pt species also exist as metallic state after reduction by H_2 at 600 °C. As shown in **Fig. 25b** and **Table 8**, the K-free PtSn@MFI gives a similar first-shell N_{Pt-Pt} of ~10.7 to the K-free Pt@MFI sample, while a first shell N_{Pt-Pt} of ~6.4 is obtained with the K-PtSn@MFI sample, giving a similar value as the K-Pt@MFI sample. These results indicate that, Sn doesn't have significant influence on the particle size of Pt in this system. Based on these results, it can be concluded that by combining the local information obtained by transmission electron microscopy and the global information obtained by X-ray absorption spectroscopy, a general description of the size distribution of Pt particles in the whole Pt-zeolite materials can be established.

Results for Tin: The chemical states and coordination environment of Sn species in the K-PtSn@MFI sample have also been studied by XAS. Firstly, the chemical state of Sn in the pristine K-PtSn@MFI-Air sample should be Sn(IV) according to the comparison with the standard SnO_2 and SnO samples (see **Fig. 25c**). After reduction by H_2, the white line intensity decreases and a red shift of the spectrum is observed in the reduced K-PtSn@MFI sample. As can be seen in **Fig. 25c**, the shape of the XANES spectra of the reduced K-PtSn@MFI resembles neither the standard Sn metal nor the standard SnO, indicating a possible formation of partially reduced SnO_{4-x} species. This deduction is also supported by the reduction in the first-shell intensity of the |FT| (**Fig. 25d**), indicating the loss of neighbouring oxygen coordinated to Sn. It can be speculated that Sn species may exist as atomically dispersed species within the K-PtSn@MFI sample on the basis of the absence of higher-shell Sn-O-Sn or Sn-Sn contribution in the EXAFS spectrum. Although we only observe the predominant first-shell Sn-O contribution in the |FT|, we could not rule out the possibility that part of the Sn species exist as subnanometric SnO_{4-x} clusters in the K-PtSn@MFI sample since the EXAFS may not be sensitive enough to detect those highly disordered species. Furthermore, to clarify whether Sn species exist as framework or extra-framework species in the K-PtSn@MFI sample, a reference Sn-Beta sample containing framework Sn species has also been measured by XAS[50,51]. As shown in **Fig. 26a** and **Fig. 26b**, it is clear that the first-shell Sn-O distance (~1.5 Å, not phase-corrected) in Sn-Beta is shorter in comparison to the other samples. Therefore, we believe that Sn atoms are not substituted in the

framework of MFI zeolite, but exist as extra-framework species in the pores and channels.

Advice for how to do the experiments: It should be noted that, all the XAS measurements for our own work were carried out under in situ conditions, meaning that the samples were treated in a reaction cell in the synchrotron beamline station before the acquisition of the XAS spectra. Specifically, the Pt-zeolite samples studied in this work were reduced by H_2 at 600 °C and then kept in H_2 flow during the measurement in order to ensure the protection of reduced Pt and Sn species from being oxidized again by air. In a recent study, we found that, small Pt particles (~1 nm) or subnanometric Pt clusters could be re-oxidized by air and show EXAFS spectra like supported isolated Pt atoms, which is probably caused by the amorphous structure of small PtOx particles[52]. Such phenomena have also been observed in other materials comprising highly dispersed Pt species[53,54]. Therefore, in order to avoid the potential misleading results and get reliable characterization results on highly dispersed metal species confined in porous materials, it is strongly recommended to perform the XAS measurements under in situ conditions.

Table 7. Fitting results of the Pt-edge EXAFS spectra of Pt@MFI-Air and K-Pt@MFI-Air.

Sample	N_{Pt-O}	R_{Pt-O} (Å)	σ^2 (Å^2)	ΔE_0 (eV)	R_{factor}
PtO_2	2 + 4	2.021 ± 0.012	0.0031 ± 0.0013	11.3 ± 1.8	0.0242
K-Pt@MFI-Air[a]	5.2 ± 0.6	1.967 ± 0.010	0.0038 ± 0.0016	6.8 ± 1.7	0.0003

Sample	N_{Pt-Pt}	R_{Pt-Pt} (Å)	σ^2 (Å^2)	ΔE_0 (eV)	R_{factor}
Pt foil	12	2.763 ± 0.001	0.0048 ± 0.0001	6.7 ± 0.5	0.0017
Pt@MFI-Air[b]	9.6 ± 1.0	2.761 ± 0.003	0.0050 ± 0.0004	7.4 ± 0.9	0.0040

[a]The fits were performed on the first coordination shell (ΔR = 1.0-2.0 Å) over |FT| of the $k^1k^2k^3$-weighted χ(k) functions performed in the Δk = 3.6-11.0 Å^{-1} interval. Non-optimized parameters are recognizable by the absence of the corresponding error bar. S_0^2=0.86.

[b]The fits were performed on the first coordination shell (ΔR = 2.0-3.0 Å) over |FT| of the $k^1k^2k^3$-weighted χ(k) functions performed in the Δk=3.6-16.7 Å^{-1} interval. The samples were fitted using a co-refinement approach resulting into one N_{Pt-Pt}, R and σ^2 for each sample and one ΔE_0 common for all samples. S_0^2=0.89

Table 8. Fitting results of Pt-edge and Sn-edge of EXAFS spectra of various Pt-zeolite materials.

Sample	N_{Pt-Pt}	R_{Pt-Pt} (Å)	σ^2 (Å^2)	ΔE_0 (eV)	R_{factor}
Pt foil	12	2.763 ± 0.001	0.0048 ± 0.0001	6.7 ± 0.5	0.0017
Pt@MFI	10.6 ± 0.6	2.762 ± 0.001	0.0051 ± 0.0002	7.0 ± 0.3	0.0025
PtSn@MFI	10.7 ± 0.4	2.763 ± 0.001	0.0050 ± 0.0001		0.0014
K-Pt@MFI	6.6 ± 1.2	2.743 ± 0.006	0.0074 ± 0.0010		0.0049
K-PtSn@MFI	6.4 ± 0.4	2.768 ± 0.001	0.0049 ± 0.0002		0.0150

Sample	N_{Sn-O}	R_{Sn-O} (Å)	σ^2 (Å^2)	ΔE_0 (eV)	R_{factor}
SnO_2	6	2.055 ± 0.010	0.0023 ± 0.0012	7.3 ± 1.4	0.0044
SnO	4	2.202 ± 0.001	0.0071 ± 0.0012	8.3 ± 0.7	0.0017
K-PtSn@MFI	3.2 ± 0.2	2.061 ± 0.006	0.0058 ± 0.0012	8.1 ± 1.0	0.0037

R, bonding distance; σ^2, Debye−Waller factor; ΔE_0, inner potential correction; R_{factor}, difference between modelled and experimental data. The fits of the Pt edge were performed on the first coordination shell (ΔR= 2.0–3.0 Å) over the Fourier transform (FT) of the $k^1k^2k^3$-weighted $\chi(k)$ functions in the range Δk= 3.6–16.7 Å^{-1} , where Δk and ΔR are the intervals in the k and R spaces for the Fourier transformation and the fit, respectively, resulting in several independent parameters of $2\Delta R\Delta k/\pi$= 39.5 (7.9 for Pt foil). Independent parameters in this work were obtained from the Artemis software as a result of a co-refinement fit of different spectra. The standard Pt foil was fitted individually while the samples were fitted using a co-refinement approach resulting in one N_{Pt-Pt}, R and σ^2 for each sample and one common ΔE_0 for all samples. The many-body amplitude reduction factor S_0^2= 0.89. The fits of the Sn edge were performed on the first coordination shell (ΔR= 1.0–2.0 Å) over the FT of the $k^1k^2k^3$-weighted $\chi(k)$ functions in the range Δk= 2.8–11.0 Å^{-1} , resulting in a number of independent parameters of $2\Delta R\Delta k/\pi$ = 20.3 for the K-PtSn@MFI sample (5.0 for both SnO_2 and SnO). SnO_2, S_0^2= 0.89; SnO, S_0^2= 1.0.

x

CO-IR

Another frequently used characterization technique to study the electronic structures of Pt species encapsulated in zeolites is in situ IR spectroscopy using CO as probe molecule. In this work, we have measured the Pt-zeolite samples by a Nexus 8700 FTIR spectrometer and a DTGS detector. The sample was reduced by H_2 in the cell for IR measurements and protected from being oxidized by air. It should be noted that, the dose of CO was controlled to be low (0.4-8.5 mbar) in order to avoid the interference of gaseous CO and the potential structural reconstruction of Pt clusters under high CO pressure. The position of the CO adsorption band in the IR spectrum is related to the electronic properties of the Pt species. As can be seen in **Fig. 27**, the CO adsorption bands at above 2000 cm^{-1} can be associated to Pt nanoparticles[55]. The IR bands at 1887 and 1719 cm^{-1}, which are observed only in the K-PtSn@MFI sample, could be related to a different cluster atomicity or different chemical composition due to the introduction of Sn into Pt clusters. As a consequence, the electronic structure of Pt species in the K-PtSn@MFI sample is different[56-59]. In particular, the CO adsorption band at 1887 cm^{-1} is probably related to the interfacial Pt-SnOx species.

Chemisorption

As a classic technique to study supported metal catalysts, chemisorption (using H_2 or CO as probe molecule) is also very useful to determine the dispersion of Pt species in zeolites. As can be seen in **Table 9**, the dispersion of Pt in various Pt-zeolite materials obtained by CO chemisorption (measured with a Quantachrome Autosorb-1C equipment) is lower than the corresponding values derived according to the average particle size obtained by STEM and EXAFS characterization results. The lower CO adsorption yield on Pt particles encapsulated in MFI zeolites has also been observed with other metal-zeolite materials in the literature[60-62]. Part of CO may be adsorbed through bridged configuration, as observed by CO-IR spectroscopy. Therefore, the adsorption stoichiometry could be lower than 1. As a result, the dispersion of Pt obtained from CO chemisorption is lower than the values obtained based on the average particle size from STEM and EXAFS results. Another point associated with the interpretation of the chemisorption results that needs to be taken into account is related to the formation of bimetallic clusters or nanoparticles, which may cause a significant decrease of the amount of gases adsorbed on metal entities. Such phenomenon has already been widely observed with

supported bimetallic nanoparticles and it can also occur with the subnanometric metal clusters confined in zeolites[63,64]. Nevertheless, the data presented in this table clearly demonstrate that, the introduction of K can significantly improve the Pt dispersion, which is associated with the formation of subnanometric Pt clusters encapsulated in MFI zeolite crystallites.

Table 9. Pt dispersion in various Pt-zeolite samples determined by CO chemisorption after calcination at 600 °C in air and subsequent reduction by H_2 at 600 °C.

Sample	Pt dispersion
Pt@MFI	10.9%
PtSn@MFI	10.3%
K-Pt@MFI	69.0%
K-PtSn@MFI	61.1%

6. Extension of the STEM-iDPC technique

In the above described protocol, we have demonstrated the structural characterization of subnanometric metal species encapsulated in purely siliceous MFI zeolite by the newly developed STEM-iDPC technique, which allows us to determine the precise location of Pt atoms and clusters in the zeolite structure. We believe this protocol can be extended to other solid materials used for heterogeneous catalysis, photocatalysis and electrocatalysis based on singly dispersed atoms or metal clusters with a few atoms[65-67]. For instance, the STEM-iDPC has been applied for identification of isolated Mo atoms in ZSM-5 zeolite[68]. In particular, porous materials like metal-organic frameworks (MOFs) are very suitable for this technique due to their sensitivity to electron beam. Under optimized imaging conditions, it can be expected that, the nodes, the organic linkers, defects as well as the metal species encapsulated inside the MOF structure can be clearly imaged, which will provide useful information to understand the details in the MOF materials at atomic and molecular level[69-71]. For example, the local structural evolution of a MIL-101 MOF sample under electron beam irradiation has been followed by STEM-iDPC, showing the subtle changes in the molecular building blocks of the MOF backbone[71]. The workflow for material synthesis and structural characterizations shown in this protocol can also be applied to other solid materials, which help to establish a reliable and

comprehensive methodology to obtain structural information at atomic level by a combination of spectroscopy and electron microscopy techniques. Understanding the limitation of each technique and retrieving useful and reliable information by complementary techniques will be vital for establishing the structure-performance relationship in catalysis as well as other applications in energy conversion and storage.

7. Limitations of current technique and outlooks

It should be noted that the different elements involved in metal-zeolite materials may distribute heterogeneously in a single crystallite of several hundred nanometres in size. The high-resolution STEM-iDPC imaging technique shown in this protocol is based on 2D projected images, which cannot reflect the whole structural information of the target material in 3D. Likewise, the 2D projected images can also cause difficulties on the data interpretation. Such limitations could be overcome by the introduction of depth sectioning analysis and high-resolution 3D electron tomography, though the spatial resolution of current TEM tomography technique needs to be improved[72,73]. Besides, the use of other techniques such as atom-probe tomography can also be quite helpful and complementary to establish 3D structural understanding on metal-zeolite materials[74].

When subnanometric metal species are encapsulated in porous materials whose thickness is over 500 nm, the contrast from the porous support will be quite high, making it quite difficult to distinguish the metal species from the support. Under these circumstances, prepare the specimen by ultramicrotomy could be an alternative way to visualize metal species located inside the porous materials. However, it should be noted that, the conventional ultramicrotomy preparation procedure involves embedding the material in resin. As a result, the thin layer of the sample (usually <100 nm) could be highly unstable under the electron beam due to the decomposition of resin, making it challenging to obtain high-resolution STEM images[75,76]. Indeed, we tried with our Pt-zeolite samples to prepare specimens by ultramicrotomy and we failed to obtained high-quality STEM-iDPC images. We expected that this problem can be solved by proper modification on the sample preparation by ultramicrotomy.

On the other hand, considering the emerging interests on two-dimensional (2D) materials in recent years and the low contrast and high beam sensitivity of the 2D support, the application of STEM-iDPC

imaging techniques for the structural characterizations of hybrid materials based on 2D structures will be quite interesting for a broad audience and should be able to provide fascinating results on the interfacial sites between the metal particles and the 2D support[77,78]. Nevertheless, we also expect the application of this technique for materials with less crystallinity and low stability under the electron beam, such as the amorphous materials widely used in catalysis[79]. Understanding the local structures at atomic level is a key to elucidate the reaction mechanism with those materials. Such attempts can also be applied to supported metal catalysts in which the metal-support interface play a dominant role in the catalytic process[80].

The capability of STEM-iDPC imaging technique working under low-dose conditions gives it the potential to be used for in situ TEM studies, in where the influence of the electron beam to the sample and reactants can be minimized and the detailed structural changes in the solid catalysts can be tracked[81,82]. Furthermore, considering the high sensitivity of iDPC technique to light elements, the STEM-iDPC imaging technique is a promising technique for direct imaging of a chemical reaction on a metal catalyst within an environmental TEM or the geometric conformation of molecules adsorbed within porous materials[83].

Another challenge for the structural characterization of the bimetallic metal clusters confined in zeolites is the direct measurement of the chemical composition by spectroscopic techniques (EDS or EELS). The low stability of the zeolite framework will cause the deformation of the zeolite structure and then lead to the random drift of the metal clusters or even their sintering. To solve that problem, the use of specific sample holders which allow to work under cryogenic conditions could contribute to minimize the beam damage effect and to stabilize the metal clusters at their anchoring positions[84,85].

As already mentioned in the introduction of this paper, the material synthesis and characterization techniques can evolve in a synergistic way. The continuous advances on the synthesis methodologies for controlling the location of metal atoms and clusters confined inside zeolite materials allow to generate metal-zeolite samples in a more uniform and precise way, which can be used as platform materials for developing the advanced TEM-based methodologies and other related characterization techniques. Structural insights at molecular and atomic level can then provide guidelines for how to improve the methods for preparing the materials. Furthermore, by continuously improving the spatial resolution of in situ TEM techniques and the related data analysis methods, the evolution of isolated

metal atoms and subnanometric metal clusters under reaction conditions can be visualized, providing direct insights on how a catalytic reaction occurs in real time[86].

References

1. Flytzani-Stephanopoulos, M. & Gates, B. C. Atomically dispersed supported metal catalysts. *Annu. Rev. Chem. Biomol. Eng.* **3**, 545-574 (2012).
2. Liu, L. & Corma, A. Metal Catalysts for Heterogeneous Catalysis: From Single Atoms to Nanoclusters and Nanoparticles. *Chem. Rev.* **118**, 4981-5079 (2018).
3. Thomas, J. M., Raja, R. & Lewis, D. W. Single-site heterogeneous catalysts. *Angew. Chem. Int. Ed.* **44**, 6456-6482 (2005).
4. Hansen, T. W. *et al.* Atomic-resolution in situ transmission electron microscopy of a promoter of a heterogeneous catalyst. *Science* **294**, 1508-1510 (2001).
5. Hwang, S., Chen, X., Zhou, G. & Su, D. In Situ Transmission Electron Microscopy on Energy-Related Catalysis. *Adv. Energy Mater.*, ASAP, doi: 10.1002/aenm.201902105 (2019).
6. Li, Z. *et al.* Well-Defined Materials for Heterogeneous Catalysis: From Nanoparticles to Isolated Single-Atom Sites. *Chem. Rev.* (2019), doi: 10.1021/acs.chemrev.9b00311.
7. Pelletier, J. D. & Basset, J. M. Catalysis by Design: Well-Defined Single-Site Heterogeneous Catalysts. *Acc. Chem. Res.* **49**, 664-677 (2016).
8. Kulkarni, A., Lobo-Lapidus, R. J. & Gates, B. C. Metal clusters on supports: synthesis, structure, reactivity, and catalytic properties. *Chem. Commun.* **46**, 5997-6015 (2010).
9. Liu, L. *et al.* Evolution and stabilization of subnanometric metal species in confined space by in situ TEM. *Nat. Commun.* **9**, 574 (2018).
10. Gates, B. C., Flytzani-Stephanopoulos, M., Dixon, D. A. & Katz, A. Atomically dispersed supported metal catalysts: perspectives and suggestions for future research. *Catal. Sci. Technol.* **7**, 4259-4275 (2017).
11. Li, H., Wang, M., Luo, L. & Zeng, J. Static Regulation and Dynamic Evolution of Single-Atom Catalysts in Thermal Catalytic Reactions. *Adv. Sci.* **6**, 1801471 (2019).
12. Liu, L. *et al.* Regioselective generation and reactivity control of subnanometric platinum clusters in zeolites for high-temperature catalysis. *Nat. Mater.* **18**, 866-873 (2019).
13. Juneau, M. *et al.* Characterization of metal-zeolite composite catalysts: Determining the environment of the active phase. *ChemCatChem*, ASAP, doi: 10.1002/cctc.201902039 (2019).
14. Shamzhy, M., Opanasenko, M., Concepcion, P. & Martinez, A. New trends in tailoring active sites in zeolite-based catalysts. *Chem. Soc. Rev.* **48**, 1095-1149 (2019).
15. Weckhuysen, B. M. Stable platinum in a zeolite channel. *Nat. Mater.* **18**, 778-779 (2019).
16. Gai, P. L. & Calvino, J. J. Electron Microscopy in the Catalysis of Alkane Oxidation, Environmental Control, and Alternative Energy Sources. *Annu. Rev. Mater. Res.* **35**, 465-504 (2005).
17. Gates, B. C. Atomically Dispersed Supported Metal Catalysts: Seeing Is Believing. *Trends Chem.* **1**, 99-110 (2019).
18. Yang, S. et al. Bridging Dealumination and Desilication for the Synthesis of Hierarchical MFI Zeolites. *Angew. Chem. Int. Ed.* 56, 12553-12556 (2017).

19. Lupulescu, A. I. & Rimer, J. D. In situ imaging of silicalite-1 surface growth reveals the mechanism of crystallization. *Science* 344, 729-732 (2014).
20. Anderson, M. W. et al. Modern microscopy methods for the structural study of porous materials. *Chem. Commun*. 907-916 (2004).
21. Mayoral, A., Carey, T., Anderson, P. A., Lubk, A. & Diaz, I. Atomic resolution analysis of silver ion-exchanged zeolite A. *Angew. Chem. Int. Ed.* 50, 11230-11233 (2011).
22. Lu, J., Aydin, C., Browning, N. D. & Gates, B. C. Imaging isolated gold atom catalytic sites in zeolite NaY. *Angew. Chem. Int. Ed.* 51, 5842-5846 (2012).
23. Ortalan, V., Uzun, A., Gates, B. C. & Browning, N. D. Direct imaging of single metal atoms and clusters in the pores of dealuminated HY zeolite. *Nat. Nanotechnol.* **5**, 506-510 (2010).
24. Yang, M. *et al.* Catalytically active Au-O(OH)x-species stabilized by alkali ions on zeolites and mesoporous oxides. *Science* **346**, 1498-1501 (2014).
25. Liu, L. *et al.* Generation of subnanometric platinum with high stability during transformation of a 2D zeolite into 3D. *Nat. Mater.* **16**, 132-138 (2017).
26. Slater, B., Ohsuna, T., Liu, Z. & Terasaki, O. Insights into the crystal growth mechanisms of zeolites from combined experimental imaging and theoretical studies. *Faraday Discussions* **136**, 125-141 (2007).
27. Diaz, I. & Mayoral, A. TEM studies of zeolites and ordered mesoporous materials. *Micron* **42**, 512-527 (2011).
28. Wan, W., Su, J., Zou, X. D. & Willhammar, T. Transmission electron microscopy as an important tool for characterization of zeolite structures. *Inorg. Chem. Frontiers* **5**, 2836-2855 (2018).
29. Mishra, R., Ishikawa, R., Lupini, A. R. & Pennycook, S. J. Single-atom dynamics in scanning transmission electron microscopy. *MRS Bulletin* **42**, 644-652 (2017).
30. DeLaRiva, A. T., Hansen, T. W., Challa, S. R. & Datye, A. K. In situ Transmission Electron Microscopy of catalyst sintering. *J. Catal.* **308**, 291-305 (2013).
31. Lazic, I., Bosch, E. G. T. & Lazar, S. Phase contrast STEM for thin samples: Integrated differential phase contrast. *Ultramicroscopy* **160**, 265-280 (2016).
32. Shen, B. *et al.* Atomic Spatial and Temporal Imaging of Local Structures and Light Elements inside Zeolite Frameworks. *Adv. Mater.* e1906103 (2019).
33. Egerton, R. F. & Watanabe, M. Characterization of single-atom catalysts by EELS and EDX spectroscopy. *Ultramicroscopy* **193**, 111-117 (2018).
34. Bonilla, G. *et al.* Zeolite (MFI) Crystal Morphology Control Using Organic Structure-Directing Agents. *Chem. Mater.* **16**, 5697-5705 (2004).
35. Karwacki, L. *et al.* Morphology-dependent zeolite intergrowth structures leading to distinct internal and outer-surface molecular diffusion barriers. *Nat. Mater.* **8**, 959-965 (2009).
36. Grand, J. *et al.* One-pot synthesis of silanol-free nanosized MFI zeolite. *Nat. Mater.* **16**, 1010-1015 (2017).
37. Varela, M. *et al.* Materials Characterization in the Aberration-Corrected Scanning Transmission Electron Microscope. *Annu. Rev. Mater. Res.* **35**, 539-569 (2005).
38. David R.G. Mitchell, Mitchell J.B. Nancarrow Probe Current Determination in Analytical TEM/STEM and Its Application to the Characterization of Large Area EDS Detectors. *Microscopy Res. Technique* **78,** 886–893 (2015).
39. R. Erni, Aberration-Corrected Imaging in Transmission Electron Microscopy. Imperial Collage Press, 2010.

40. Díaz, I., Kokkoli, E., Terasaki, O. & Tsapatsis, M. Surface Structure of Zeolite (MFI) Crystals. *Chem. Mater.* **16**, 5226-5232 (2004).
41. Barthel, J. Dr. Probe: A software for high-resolution STEM image simulation. *Ultramicroscopy* **193**, 1-11 (2018).
42. De Wael, A., De Backer, A., Jones, L., Nellist, P. D. & Van Aert, S. Hybrid statistics-simulations based method for atom-counting from ADF STEM images. *Ultramicroscopy* **177**, 69-77 (2017).
43. Hwang, J., Zhang, J. Y., D'Alfonso, A. J., Allen, L. J. & Stemmer, S. Three-dimensional imaging of individual dopant atoms in $SrTiO_3$. *Phys Rev Lett* **111**, 266101 (2013).
44. S. Bernal, F. J. Botana, J. J. Calvino, C. López-Cartes, J. A. Pérez-Omil, J. M. Rodríguez-Izquierdo, The interpretation of HREM images of supported metal catalysts using image simulation: profile view images. *Ultramicroscopy* **72**, 135-164 (1998).
45. E. J. Kirkland, *Advanced Computing in Electron Microscopy*. Springer, 2010.
46. Corma, A., Fornes, V., Pergher, S. B., Maesen, T. L. M. & Buglass, J. G. Delaminated zeolite precursors as selective acidic catalysts. *Nature* **396**, 353-356 (1998).
47. Pei, Y. *et al.* Catalytic properties of intermetallic platinum-tin nanoparticles with non-stoichiometric compositions. *J. Catal.* **374**, 136-142 (2019).
48. Moliner, M. *et al.* Reversible Transformation of Pt Nanoparticles into Single Atoms inside High-Silica Chabazite Zeolite. *J. Am. Chem. Soc.* **138**, 15743-15750 (2016).
49. de Graaf, J., van Dillen, A. J., de Jong, K. P. & Koningsberger, D. C. Preparation of Highly Dispersed Pt Particles in Zeolite Y with a Narrow Particle Size Distribution: Characterization by Hydrogen Chemisorption, TEM, EXAFS Spectroscopy, and Particle Modeling. *J. Catal.* **203**, 307-321 (2001).
50. Bare, S. R. *et al.* Uniform catalytic site in Sn-beta-zeolite determined using X-ray absorption fine structure. *J. Am. Chem. Soc.* **127**, 12924-12932 (2005).
51. Hammond, C. *et al.* Identification of Active and Spectator Sn Sites in Sn-beta Following Solid-State Stannation, and Consequences for Lewis Acid Catalysis. *ChemCatChem* **7**, 3322-3331 (2015).
52. Liu, L. *et al.* Determination of the Evolution of Heterogeneous Single Metal Atoms and Nanoclusters under Reaction Conditions: Which Are the Working Catalytic Sites? *ACS Catal.* **9**, 10626-10639 (2019).
53. Derevyannikova, E. A. *et al.* Structural Insight into Strong Pt–CeO_2 Interaction: From Single Pt Atoms to PtOx Clusters. *J. Phys. Chem. C* **123**, 1320-1334 (2018).
54. Sun, Q. *et al.* Subnanometer Bimetallic Pt-Zn Clusters in Zeolites for Propane Dehydrogenation. *Angew. Chem. Int. Ed.* (2020), doi: 10.1002/anie.202003349.
55. Concepcion, P. *et al.* The promotional effect of Sn-beta zeolites on platinum for the selective hydrogenation of alpha,beta-unsaturated aldehydes. *Phys. Chem. Chem Phys.* **15**, 12048-12055 (2013).
56. Heiz, U., Sanchez, A., Abbet, S., Schneider, W. D. Catalytic Oxidation of Carbon Monoxide on Monodispersed Platinum Clusters: Each Atom Counts. *J. Am. Chem. Soc.* **121**, 3214-3217 (1999).
57. Serykh, A. I. *et al.* Stable subnanometre Pt clusters in zeolite NaX via stoichiometric carbonyl complexes: Probing of negative charge by DRIFT spectroscopy of adsorbed CO and H_2. *Phys. Chem. Chem. Phys.* **2**, 5647-5652 (2000).
58. Drozdová, L. *et al.* Subnanometer platinum clusters in zeolite NaEMT via stoichiometric carbonyl clusters. *Microporous Mesoporous Mater.* **35-36**, 511-519 (2000).
59. Mishra, D. K., Dabbawala, A. A. & Hwang, J.-S. Ruthenium nanoparticles supported on zeolite Y

as an efficient catalyst for selective hydrogenation of xylose to xylitol. *J. Mol. Catal. A: Chem.* **376**, 63-70 (2013).
60. Visser, T. *et al.* Promotion effects in the oxidation of CO over zeolite-supported Pt nanoparticles. *J. Phys. Chem. B* **109**, 3822-3831 (2005).
61. Rivallan, M. *et al.* Platinum sintering on H-ZSM-5 followed by chemometrics of CO adsorption and 2D pressure-jump IR spectroscopy of adsorbed species. *Angew. Chem. Int. Ed.* **49**, 785-789 (2010).
62. Balakrishnan, K. A chemisorption and XPS study of bimetallic Pt-Sn/Al_2O_3 catalysts. *J. Catal.* **127**, 287-306 (1991).
63. Panja, C. & Koel, B. E. Probing the Influence of Alloyed Sn on Pt(100) Surface Chemistry by CO Chemisorption. *Israel J. Chem.* **38**, 365-374 (1998).
64. Chen, Y. *et al.* Single-Atom Catalysts: Synthetic Strategies and Electrochemical Applications. *Joule* **2**, 1242-1264 (2018).
65. Wang, A., Li, J. & Zhang, T. Heterogeneous single-atom catalysis. *Nat. Rev. Chem.* **2**, 65-81 (2018).
66. Zhang, H., Liu, G., Shi, L. & Ye, J. Single-Atom Catalysts: Emerging Multifunctional Materials in Heterogeneous Catalysis. *Adv. Energy Mater.* **8**, 1701343 (2018).
67. Wiktor, C., Meledina, M., Turner, S., Lebedev, O. I. & Fischer, R. A. Transmission electron microscopy on metal–organic frameworks – a review. *J. Mater. Chem. A* **5**, 14969-14989 (2017).
68. Liu, L. *et al.* Direct Imaging of Atomically Dispersed Molybdenum that Enables Location of Aluminum in the Framework of Zeolite ZSM-5. *Angew. Chem. Int. Ed.* **59**, 819-825 (2020).
69. Zuo, Q. *et al.* Ultrathin Metal-Organic Framework Nanosheets with Ultrahigh Loading of Single Pt Atoms for Efficient Visible-Light-Driven Photocatalytic H_2 Evolution. *Angew. Chem. Int. Ed.* **58**, 10198-10203 (2019).
70. Liu, L. *et al.* Imaging defects and their evolution in a metal-organic framework at sub-unit-cell resolution. *Nat. Chem.* **11**, 622-628 (2019).
71. Zhou, Y. *et al.* Local structure evolvement in MOF single crystals unveiled by scanning transmission electron microscopy. *Chem. Mater.* (2020).
72. Borisevich, A. Y., Lupini, A. R. & Pennycook, S. J. Depth sectioning with the aberration-corrected scanning transmission electron microscope. *Proc. Natl. Acad. Sci. USA* **103**, 3044-3048 (2006).
73. Zecevic, J., van der Eerden, A. M., Friedrich, H., de Jongh, P. E. & de Jong, K. P. Heterogeneities of the nanostructure of platinum/zeolite y catalysts revealed by electron tomography. *ACS Nano* **7**, 3698-3705 (2013).
74. Schmidt, J. E., Oord, R., Guo, W., Poplawsky, J. D. & Weckhuysen, B. M. Nanoscale tomography reveals the deactivation of automotive copper-exchanged zeolite catalysts. *Nat. Commun.* **8**, 1666 (2017).
75. Chen, Z. *et al.* Direct synthesis of core-shell MFI zeolites with spatially tapered trimodal mesopores via controlled orthogonal self-assembly. *Nanoscale* **11**, 16667-16676 (2019).
76. Kliewer, C. E. Electron Microscopy and Imaging, in *Zeolite Characterization and Catalysis*, Chester, A.W., Derouane, E.G. (eds.), Springer, 2009.
77. Deng, D. *et al.* Catalysis with two-dimensional materials and their heterostructures. *Nat. Nanotechnol.* **11**, 218-230 (2016).
78. Li, Z. *et al.* Reactive metal–support interactions at moderate temperature in two-dimensional niobium-carbide-supported platinum catalysts. *Nat. Catal.* **1**, 349-355 (2018).
79. Goldsmith, B. R., Peters, B., Johnson, J. K., Gates, B. C. & Scott, S. L. Beyond Ordered Materials:

Understanding Catalytic Sites on Amorphous Solids. *ACS Catal.* **7**, 7543-7557 (2017).
80. van Deelen, T. W., Hernández Mejía, C. & de Jong, K. P. Control of metal-support interactions in heterogeneous catalysts to enhance activity and selectivity. *Nat. Catal.* **2**, 955-970 (2019).
81. Hodnik, N., Dehm, G. & Mayrhofer, K. J. Importance and Challenges of Electrochemical in Situ Liquid Cell Electron Microscopy for Energy Conversion Research. *Acc. Chem. Res.* **49**, 2015-2022 (2016).
82. Boyes, E. D., LaGrow, A. P., Ward, M. R., Mitchell, R. W. & Gai, P. L. Single Atom Dynamics in Chemical Reactions. *Acc. Chem. Res.* **53**, 390-399 (2020).
83. Nakamura, E. Atomic-Resolution Transmission Electron Microscopic Movies for Study of Organic Molecules, Assemblies, and Reactions: The First 10 Years of Development. *Acc. Chem. Res.* **50**, 1281-1292 (2017).
84. Li, T. *et al.* Cryo-TEM and electron tomography reveal leaching-induced pore formation in ZSM-5 zeolite. *J. Mater. Chem. A* **7**, 1442-1446 (2019).
85. Li, Y. *et al.* Cryo-EM Structures of Atomic Surfaces and Host-Guest Chemistry in Metal-Organic Frameworks. *Matter* **1**, 428-438 (2019).
86. Liu, L. & Corma, A. Evolution of Isolated Atoms and Clusters in Catalysis. *Trends Chem.* **2**, 383-400 (2020).

Reporting Summary

Further information on experimental design is available in the Nature Research Reporting Summary linked to this article.

Data availability

Data supporting this publication are available from the corresponding author upon request.

Code Availability

The code and scripts used in this work are available from the corresponding author upon request.

Competing interests

The authors declare no competing interests.

Author Contributions

A.C. conceived the project and directed the study. L.L. carried out the synthesis and characterizations of the Pt-zeolite materials. M.L.-H. and J.J.C. carried out the high-resolution STEM measurements,

image analysis and simulations with assistance from L.L. All the authors discussed the results and contributed to the formation of the manuscript.

Acknowledgements

This work has been supported by the European Union through the European Research Council (grant ERC-AdG-2014-671093, SynCatMatch) and the Spanish government through the "Severo Ochoa Program" (SEV-2016-0683). The authors also thank Microscopy Service of UPV for the TEM and STEM measurements. The XAS measurements were carried out in CLAESS beamline of ALBA synchrotron. High-resolution STEM measurements were performed at the DME-UCA node of the ELECMI Singular Infrastructure (ICTS) in Cadiz University, with financial support from FEDER/MINECO (MAT2017-87579-R and MAT2016-81118-P). The financial support from ExxonMobil on this project is also greatly acknowledged.

Related links

Key reference(s) using this protocol

Liu, L. *et al. Nat. Mater.* 18, 866-873 (2019) [https://www.nature.com/articles/s41563-019-0412-6]

Key data used in this protocol

Liu, L. *et al. Nat. Mater.* 18, 866-873 (2019) [https://www.nature.com/articles/s41563-019-0412-6]

FIGURE:

Fig. 1| One-pot synthesis of Pt-zeolite materials. (a, b) Schematic illustration of formation process of Pt@MFI and K-Pt@MFI samples by one-pot synthesis. The only difference between the two preparation methods is the presence of K^+ in the starting synthesis mixture. For the preparation of PtSn@MFI and K-PtSn@MFI samples, a Sn source ($SnCl_4 \cdot 5H_2O$) will be added in the synthesis mixture. OSDA, organic structure-directing agent.

Fig. 2| XRD patterns of the Pt-MFI zeolites with different chemical compositions. Typical diffraction patterns corresponding to MFI zeolite are observed in all the samples.

Fig. 3| FESEM images of Pt-zeolite materials. (a) K-free Pt@MFI, (b) K-free PtSn@MFI, (c) K-Pt@MFI and (d) K-PtSn@MFI.

Fig. 4| HAADF-STEM images of K-Free Pt@MFI-Air sample after calcination in air. A large number of Pt nanoparticles can be observed in this sample.

Fig. 5| HAADF-STEM images of K- Pt@MFI-Air sample after calcination in air. No Pt clusters are observed in these STEM images recorded on a conventional TEM. Some lattice fringes can be seen in the high-magnification STEM images. However, the resolution and contrast are not enough to identify the presence of very tiny Pt species in this sample.

Fig. 6| HAADF-STEM images of K-free Pt@MFI sample after calcination in air at 600 °C and then further reduction by H_2 at 600 °C. A large number of Pt nanoparticles can be observed in this sample.

Fig. 7| HAADF-STEM images of K-Pt@MFI sample after calcination in air at 600 °C and then further reduction by H_2 at 600 °C. The lattice fringes of MFI zeolite can be observed in the high-

magnification STEM images and the size of the subnanometric Pt clusters can also be estimated according to these images.

Fig. 8| STEM image of Pt-zeolite samples after reduction by H_2 at 600 °C. K-free Pt-MFI (a), K-Pt@MFI (b), K-free PtSn@MFI (c) and K-PtSn@MFI (d). The size distributions of Pt particles in different Pt-zeolite materials are presented: K-free Pt-MFI (e), K-Pt@MFI (f), K-free PtSn@MFI (g) and K-PtSn@MFI (h). More than 200 particles were counted. The average particle size is calculated according to $d= \Sigma n_i d_i^3/\Sigma n_i d_i^2$.

Fig. 9| Workflow of characterization of metal-zeolite materials by STEM-iDPC.

Fig. 10| Stability test of the K-PtSn@MFI sample under the beam. (a) HAADF-STEM image and (b) corresponding iDPC image of a typical area of the K-PtSn@MFI sample containing subnanometric Pt clusters. After the first scan, STEM and iDPC images were recorded consecutively in a second (c, d), third (e, f) and fourth scan (g, h). The beam damage on the zeolite structure can be observed in the third and fourth scans, which are indicated in the iDPC images by red circles. The color gradient bar indicates the contrast in the HAADF-STEM images.

Fig. 11| Influence of defocus value on the imaging of isolated Pt atoms. Image simulation results of single Pt atoms in different positions of MFI zeolite (in straight pore channel, sinusoidal channel or in the intersectional void) along the [010] direction. The influence of defocus has also been studied. The image intensity values (color scale on the right) are expressed in terms of the fraction of incident beam.

Fig. 12| Influence of defocus value on the imaging of isolated Sn atoms. Image simulation results of single Sn atoms in different positions of MFI zeolite (in straight pore channel, sinusoidal channel or in the intersectional void) along the [010] direction. The influence of defocus has also been studied. The image intensity values (color scale on the right) are expressed in terms of the fraction of incident beam.

Fig. 13| Image simulation of isolated Pt and Sn atoms in MFI zeolite. Image simulation results of single Pt and Sn atoms in different positions of MFI zeolite (in straight pore channel, sinusoidal channel or in the intersectional void) along the [010] direction. The intensity (fraction of incident electron beam) of the corresponding position in the zeolite framework is also plotted as a reference.

Fig. 14| Image simulation of Pt and Sn species in MFI zeolite. Image simulation details of different types of Pt single atom (Pt-s), Pt clusters (Pt-c), Sn single atom (Sn-s) and Sn clusters (Sn-c) in the MFI zeolite along [010] direction. (a) structural model implementing both Pt and Sn isolated atoms and clusters; (b) HR HAADF STEM simulated image; (c) simulated HR HAADF STEM image after addition of Poisson and white Gaussian noise; (d) UWT denoised image; (e) background subtracted and denoised image.

Fig. 15| Image simulation of Pt and Sn species in MFI zeolite. Image simulation details of different types of Pt single atom (Pt-s), Pt clusters (Pt-c), Sn single atom (Sn-s) and Sn clusters (Sn-c) in the MFI zeolite along tilted-[010] direction. (a) structural model implementing both Pt and Sn isolated atoms and clusters; (b) HR HAADF STEM simulated image; (c) simulated HR HAADF STEM image after addition of Poisson and white Gaussian noise; (d) UWT denoised image; (e) background subtracted and denoised image.

Fig. 16| Image simulation of Pt clusters comprising interaction with Sn species in MFI zeolite. Image simulation results from structural models of subnanometric Pt clusters and contacted Pt and Sn clusters (as described in each simulation). A shoulder appears in the intensity profile when the Pt cluster is in contact with a Sn cluster. If Pt cluster is in contact with a single Sn atom, it will be quite difficult to identify such type of structure, according to our simulation results.

Fig. 17| Characterization of K-Pt@MFI-Air sample by STEM-iDPC imaging technique. HR HAADF-STEM images (a, c) and the corresponding iDPC images (b, d) of K-Pt@MFI-Air sample, showing the presence of atomically dispersed Pt species in MFI zeolite and their location in the zeolite

structure. By correlating the HR HAADF-STEM and corresponding iDPC images, the location of isolated Pt atoms can be determined to be in the 10MR sinusoidal channels, as indicated by red dots in (b) and (d). The color gradient bar indicates the contrast in the HAADF-STEM images. As discussed in the manuscript, it is possible to identify a single Pt atom from the zeolite framework. However, the contrast of the single Pt atom is not as clear as the Pt clusters. Considering the contrast in the HAADF-STEM image may be influence by the depth of Pt atom, defects in the MFI zeolite structure and random noise, we only attempt the assign the atoms with high contrast in the HAADF-STEM images while those Pt atoms with "moderate" contrast is not assigned.

Fig. 18| Identification of the location of subnanometric Pt clusters within the MFI structure. (a, c) Large-area and detailed high-resolution HAADF-STEM image and (b, d) the corresponding iDPC image of the same area of K-Pt@MFI sample in the [010] orientation. (e, g) Large-area and detailed HAADF-STEM image and (f, h) the corresponding iDPC image of the same area of K-Pt@MFI sample in the tilted-[010] orientation. (i, k) Large-area and detailed high-resolution HAADF-STEM image and (j, l) the corresponding iDPC image of the same area of K-PtSn@MFI sample in the [010] orientation. (m, o) Large-area and detailed HAADF-STEM image and (n, p) the corresponding iDPC image of the same area of K-PtSn@MFI sample in the tilted-[010] orientation. In the HAADF-STEM images, subnanometric Pt clusters (~0.5 nm) are clearly imaged. In the corresponding iDPC images, the atomic structures of MFI zeolite are also clearly revealed. By combing the images obtained in the two modes, we can identify the precise location of Pt species in the MFI zeolite, corresponding to the sinusoidal channels. The color gradient bar indicates the contrast in the HAADF-STEM images.

Fig. 19| Correlation between the simulated image and experimental STEM-iDPC images. (a) Simulated HAADF-STEM image along the [010] orientation, showing the contrast of different types of Pt and Sn species. (b, c) Experimental HAADF-STEM and corresponding iDPC image of a K-PtSn@MFI-600H_2 sample containing Pt and Sn clusters along the [010] orientation. In (b), the particles with high contrast are ascribed to Pt clusters while the particles with lower contrast are ascribed to Sn clusters. Due to the very low contras of Pt atom and Sn atom, those isolated atoms are not identified. (d) Simulated HAADF-STEM image along the tilted-[010] orientation, showing the contrast Pt and Sn

clusters. (e, f) Experimental HAADF-STEM and corresponding iDPC image of a K-PtSn@MFI-600H_2 sample containing Pt and Sn clusters along the tilted-[010] orientation. In (e), the particles with high contrast are ascribed to Pt clusters while the particles with lower contrast are ascribed to Sn clusters. Due to the very low contrasts of Pt atom and Sn atom, those isolated atoms are not identified.

Fig. 20| Chemical analysis on the K-PtSn@MFI sample by EDS. (a-f) Elemental mapping of K-PtSn@MFI sample, showing the homogeneous distributions of K, Sn and Pt in the zeolite crystallites. Due to the limitation of EDS, it is not able to clarify the spatial distribution of Pt and Sn at atomic level.

Fig. 21| K-means clustering analysis on the simulated images. (a) Model of MFI zeolite containing Sn atom, Pt atom, Sn clusters and Pt clusters along the [010] orientation. (b) Simulated HAADF-STEM image of the model shown in (a). (c) Unsupervised K-means clustering analysis on the simulated HAADF-STEM image, showing the identification of Sn and Pt clusters. However, the identification of Pt single atom and Sn atom will be quite difficult due to their low contrast, especially for isolated Sn atom. (d) Model of MFI zeolite containing Sn atom, Pt atom, Sn clusters and Pt clusters along the tilted-[010] orientation. (e) Simulated HAADF-STEM image of the model shown in (d). (f) Unsupervised K-means clustering analysis on the simulated HAADF-STEM image, showing the identification of Sn and Pt clusters. However, the identification of Pt single atom and Sn atom will be quite difficult due to their low contrast, especially for isolated Sn atom. Herein, considering the appearance of noise should be random in the experimental images, we have performed the K-means clustering analysis based on four simulated images with the same amount of total noise but different distributions, as shown in (c) and (f).

Fig.22| Distinguishing subnanometric Pt and Sn species by K-means clustering analysis. (a) High-resolution HAADF-STEM image of K-PtSn@MFI sample along the tilted [010] direction. The contrasts of the subnanometric particles are displayed in pseudo color for improved visualization. (b) Automatic identification of the subnanometric Pt (red) and Sn (green) species using segmentation by K-means clustering. The contrast information in the simulation results was taken into account. (c)

Location of Pt (red) and Sn (green) species with distance below 0.1 nm, which may establish interaction between them. The statistical analysis shows that, ~40% of the Pt clusters in this area are in contact with Sn species.

Fig. 23| PtSn clusters in experimental HAADF-STEM images. Details of different areas in the experimental HR HAADF STEM images of K-PtSn@MFI sample, illustrating the presence of possible contacts between Pt and Sn clusters. These experimental STEM images are consistent with the simulation results in **Fig. 18**. It should be noted that, the contrast of the subnanometric metal cluster could be influenced by several factors, such as the atomicity, chemical composition, geometric configuration. Therefore, the assignment of the Pt and Sn domains in this figure could be complicated. The results shown in this figure are speculative on the basis of the simulation results.

Fig. 24| Characterization of the Pt-zeolite materials after calcination in air (Pt@MFI-Air and K-Pt@MFI-Air) by XAS. Fitting of the EXAFS spectrum of Pt@MFI-Air in k^1 (c) and k^3 space (e). Fitting of the EXAFS spectrum of K-Pt@MFI-Air in k^1 (d) and k^3 space (f).

Fig. 25| Characterization of Pt-zeolite materials by XAS. All the samples are *in situ* reduced by H_2 at 600 ^oC before the spectra collection, except for the K-PtSn@MFI-Air sample in (c), which was measured directly without pre-reduction by H_2. The Pt and Sn standard samples were also measured directly. XANES spectra (a) and EXAFS spectra (b) of Pt L_3-edge of different Pt-zeolite samples. (c) Sn K-edge XANES spectra of K-PtSn@MFI-Air and K-PtSn@MFI sample. (d) Sn K-edge EXAFS spectrum of K-PtSn@MFI sample.

Fig. 26| Comparison of the Sn-edge XAS results of K-PtSn@MFI-Air sample with Sn-Beta. (a) k-space Sn-edge EXAFS spectra and (b) R-space of Sn-edge EXAFS spectra of Sn-Beta, K-PtSn@MFI-Air (pristine sample after calcination in air at 600 ^oC), K-PtSn@MFI-H_2 (sample after in situ reduction by H_2 at 600 ^oC) and SnO_2 reference. The EXAFS signal of Sn-Beta in k space is rather different in comparison with those from the SnO_2 standard sample and K-PtSn@MFI-Air and K-PtSn@MFI-H_2 samples, indicating the different Sn coordination environment. Notably, as shown in

the |FT| spectra (b), it is clear that the first-shell Sn-O distance (~1.5 Å, not phase-corrected) in Sn-Beta is shorter in comparison to the other samples. Therefore, from a XAS perspective, we believe Sn atoms are not substituted in the framework of MFI zeolite, but exist as extra-framework species in the channels of MFI zeolite structure.

Fig. 27| CO-IR spectra of K-PtSn@MFI and K-Pt@MFI samples. The band at 2042 cm^{-1} correspond to lineal bonded CO to Pt nanoparticles, while the bands at 1693 to 1887 cm^{-1} can be associated to Co adsorbed on Pt clusters. Assignation of the IR bands to Pt carbonyl species has been verified by ^{13}CO IR adsorption studies, where the corresponding shift to ~50 cm^{-1} lower wavenumbers have been observed.